

STUDIES OF THE JET IN BL LACERTAE. II. SUPERLUMINAL ALFVÉN WAVES

M. H. COHEN¹, D. L. MEIER^{1,2}, T. G. ARSHAKIAN^{3,4}, E. CLAUSEN-BROWN⁵, D. C. HOMAN⁶, T. HOVATTA^{7,1}, Y. Y. KOVALEV^{8,5},
M.L. LISTER⁹, A. B. PUSHKAREV^{10,11,5}, J. L. RICHARDS⁹, T. SAVOLAINEN^{5,7}

(Received September 10, 2014)

ABSTRACT

Ridge lines on the pc-scale jet of the active galactic nucleus BL Lac display transverse patterns that move superluminally downstream. The patterns are not ballistic, but are analogous to waves on a whip. Their apparent speeds β_{app} (units of c) range from 4.2 to 13.5, corresponding to $\beta_{\text{wave}}^{\text{gal}} = 0.981 - 0.998$ in the galaxy frame. We show that the magnetic field in the jet is well-ordered with a strong transverse component, and assume that it is helical and that the transverse patterns are longitudinal Alfvén waves. The wave-induced transverse speed of the jet is non-relativistic ($\beta_{\text{tr}}^{\text{gal}} \sim 0.09$) and in agreement with our assumption of low-amplitude waves. In 2010 the wave activity subsided and the jet displayed a mild wiggle that had a complex oscillatory behavior. The waves are excited by changes in the position angle of the recollimation shock, in analogy to exciting a wave on a whip by shaking it. Simple models of the system are presented; the preferred one assumes that the sound speed in the plasma is $\beta_s = 0.3$ and this, combined with the measured speeds of the Alfvén wave and a component that is assumed to be an MHD slow wave, results in Lorentz factor of the jet $\Gamma_{\text{jet}} \sim 2.8$, pitch angle of the helix (in the jet frame) $\alpha \sim 43^\circ$, Alfvén speed $\beta_A \sim 0.86$, and magnetosonic Mach number $M_{\text{ms}} \sim 1.5$. This describes a plasma in which the magnetic field is dominant but not overwhelmingly so, and the field is in a moderate helix.

Keywords: BL Lacertae objects:individual (BL Lacertae) – galaxies:active – galaxies: jets – magnetohydrodynamics (MHD) – waves

1. INTRODUCTION

This is the second in a series of papers in which we study high-resolution images of BL Lacertae made at 15 GHz with the VLBA, under the MOJAVE program (Monitoring of Jets in Active Galactic Nuclei with VLBA Experiments, Lister et al., 2009). In Cohen et al. (2014, hereafter Paper I) we investigated a quasi-stationary jet component located 0.26 mas from the core, (0.34 pc, projected) and identified it as a recollimation shock (RCS). Numerous bright radio features (components) appear to emanate from this shock, or pass through it. They propagate superluminally downstream, and their tracks cluster around an axis that connects the core and the RCS. This behavior is highly similar to the results of numerical modeling (Lind et al. 1989; Meier 2012), in which MHD waves or shocks are emitted by an RCS. In the simulations, the jet has a magnetic field that dominates the dynamics, and

is in the form of a helix with a high pitch angle, α . In BL Lac the motions of the components are similar to those in the numerical models, and in addition the Electric Vector Position Angle (EVPA) is longitudinal; i.e., parallel to the jet axis. For a jet dominated by helical field, this indicates that the toroidal component dominates the poloidal component, a necessary condition for the comparison of the observations with the numerical simulations. Hence, in Paper I, we assumed that the superluminal components in BL Lac are compressions in the beam established by slow- and/or fast- mode magnetosonic waves or shocks traveling downstream on a helical field.

It has been common to assume that the EVPA is perpendicular to the projection of the magnetic field vector B that is in the synchrotron emission region. This is correct in the frame of an optically-thin emission region, but may well be incorrect in the frame of the observer if the beam is moving relativistically (Blandford & Königl 1979; Lyutikov, Pariev, & Gabuzda 2005). Lyutikov, Pariev, & Gabuzda (2005) show that if the jet is cylindrical and not resolved transversely, and if the B field has a helical form, then the EVPA will be either longitudinal or perpendicular to the jet, depending on the pitch angle. This is partly seen in the polarization survey results of Lister & Homan (2005), where the BL Lac objects tend to have longitudinal EVPA in the inner jet, whereas the quasars have a broad distribution of EVPA, relative to the jet direction. This suggests that in BL Lacs the field may be helical, with pitch angles large enough to produce longitudinal polarization, although strong transverse shocks in a largely tangled field are also a possibility (e.g. Hughes 2005). The wide distribution of EVPA values in quasars suggests that oblique shocks, rather than helical structures, might dominate the field order. However, a distribution of helical pitch angles could also explain the EVPAs in quasars, if symmetry is broken between the near and far sides of the

¹ Department of Astronomy, California Institute of Technology, Pasadena, CA 91125, USA; mhc@astro.caltech.edu

² Jet Propulsion Laboratory, California Institute of Technology, Pasadena, CA 91109 USA

³ I. Physikalisches Institut, Universität zu Köln, Zùlpicher Strasse 77, 50937 Köln, Germany

⁴ Byurakan Astrophysical Observatory, Byurakan 378433, Armenia and Isaac Newton Institute of Chile, Armenian Branch

⁵ Max-Planck-Institut für Radioastronomie, Auf dem Hügel 69, 53121 Bonn, Germany

⁶ Department of Physics, Denison University, Granville, OH 43023 USA

⁷ Aalto University Metsähovi Radio Observatory, Metsähovintie 114, 02540 Kylmäla, Finland

⁸ Astro Space Center of Lebedev Physical Institute, Profsoyuznaya 84/32, 117997 Moscow, Russia

⁹ Department of Physics, Purdue University, 525 Northwestern Avenue, West Lafayette, IN 47907, USA

¹⁰ Pulkovo Observatory, Pulkovskoe Chausee 65/1, 196140 St. Petersburg, Russia

¹¹ Crimean Astrophysical Observatory, 98409 Nauchny, Crimea, Ukraine

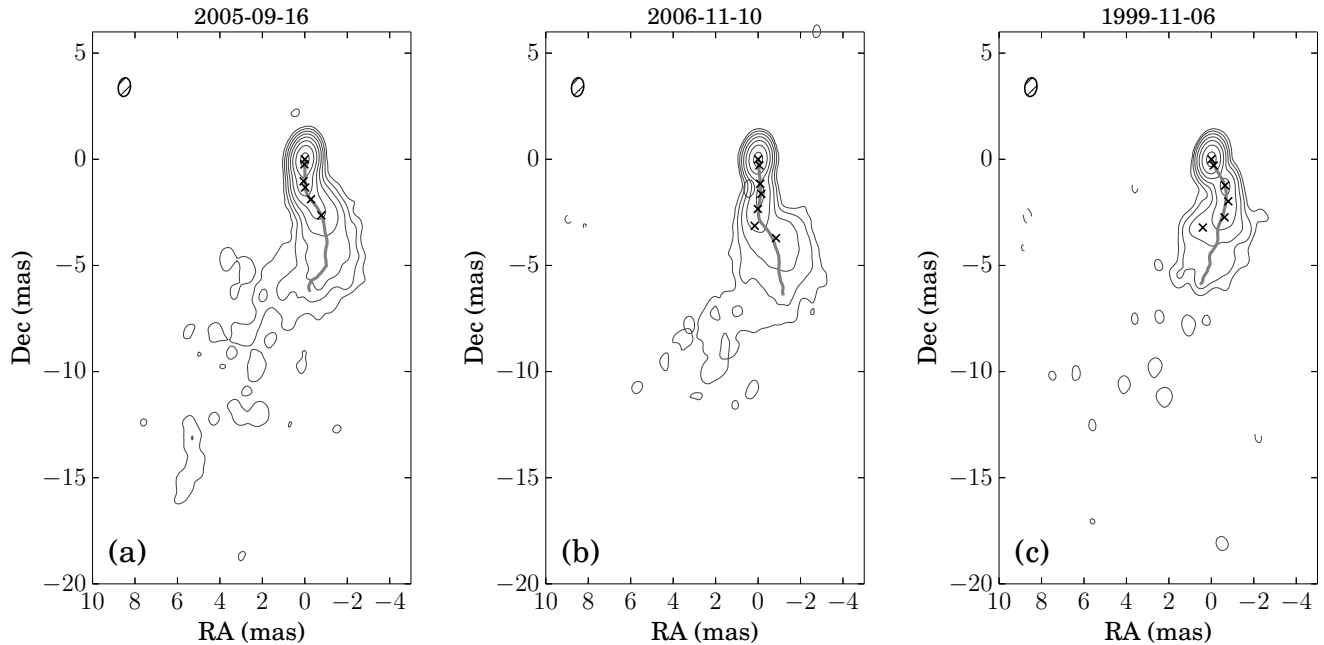


Figure 1. 15 GHz VLBA images of BL Lac with ridge line and components (the crosses). In (a) the components lie close to the ridge line. In (b) the three outer components are off the ridge line by up to 0.3 mas. In this case the true ridge has a sharp bend and the algorithm has difficulty in following it. In (c) the ridge has a step near the core, and appears to bifurcate downstream. The algorithm misses the step, and is unable to deal with the bifurcation.

jet. It has been suggested (Meier 2013) that this difference in the magnetic field is fundamental to the generic differences between quasars and BL Lacs.

BL Lacs often show a bend in the jet, and the literature contains examples showing that in some cases the EVPA stays longitudinal around the bend; e.g., 1803+784; Gabuzda (1999), 1749+701; Gabuzda & Pushkarev (2001), and BL Lac itself; O’Sullivan & Gabuzda (2009). In these examples and in other BL Lacs studied in the MOJAVE program¹², the fractional polarization rises smoothly along the jet to values as high as 30%. The field must be well-ordered for the polarization to be that high. We assume that the field is in a rather tight helix (in the beam frame) and that the moving patterns (the bends) are Alfvén waves propagating along the longitudinal component of the field.

In a plasma dominated by the magnetic field, Alfvén waves are transverse displacements of the field (and, perforce, of the plasma), analogous to waves on a whip. The tension is provided by the magnetic field ($\propto B^2$), and the wave velocity is proportional to the square root of the tension divided by the density. Alfvén waves have been employed in various astronomical contexts, including the acceleration of cosmic rays (Fermi 1949), the solar wind (Belcher, Davis & Smith 1969), the Jupiter-Io system (Belcher 1987), turbulence in the ISM (Goldreich & Sridhar 1997), the bow shock of Mars (Edberg et al. 2010), and the solar atmosphere (McIntosh et al. 2011). In our case they are transverse waves on a relativistically-moving beam of plasma threaded with a helical magnetic field. The appropriate formulas for the phase speeds of the MHD waves are given in the Appendix of Paper I.

Changes in the bends of BL Lacs are also seen frequently. Britzen et al. (2010a) showed that in 1.4 years the ridge line in 0735+178 changed from having a “staircase” structure

to being straight, and that there were prominent transverse motions. Britzen et al. (2010b) also studied 1803+784 and described various models that might explain the structure. Perucho et al. (2012) studied the ridge line in 0836+710 at several frequencies and over a range of epochs. They showed that the ridge line corresponds to the maximum pressure in the jet. They discussed the concept of transverse velocity, and concluded that their measured transverse motions are likely to be caused by a “moving wave pattern”; this was elaborated in Perucho (2013). In our work here on BL Lac we also see transverse motions, but their patterns move longitudinally and we identify them as Alfvén waves. We calculate the resulting transverse velocity of the jet and show that it is non-relativistic.

It has been more customary to discuss the fast radio components in a relativistic jet in hydrodynamic (HD) terms. We note here only a few examples of this. The shock-in-jet model (Marscher & Gear 1985; Marscher 2014) was used by Hughes, Aller, & Aller (1989a, 1989b, 1991) to develop models of several sources, including BL Lac (Hughes, Aller, & Aller 1989b) and 3C 279 (Hughes, Aller, & Aller 1991). Lobanov & Zensus (2001) recognized two threads of emission in 3C 273 that they explained with Kelvin-Helmholtz (KH) instabilities, and this was developed more by Perucho et al. (2006). Hardee, Walker & Gómez (2005) discussed the patterns and motions in 3C 120 in terms of helical instability modes. In all these studies the magnetic field is needed of course for the synchrotron radiation, but it also is explicitly used to explain observed polarization changes as due to compression of the transverse components of magnetic field, by the HD shock. But the magnetic field has no dynamical role in the jet. On the contrary, in this paper, as in Paper I, we assume that the dynamics in the jet are dominated by the magnetic field.

The plan for this paper is as follows. In Section 2 we briefly describe the observations. The definition of the ridge line of

¹² <http://www.physics.purdue.edu/astro/MOJAVE/>

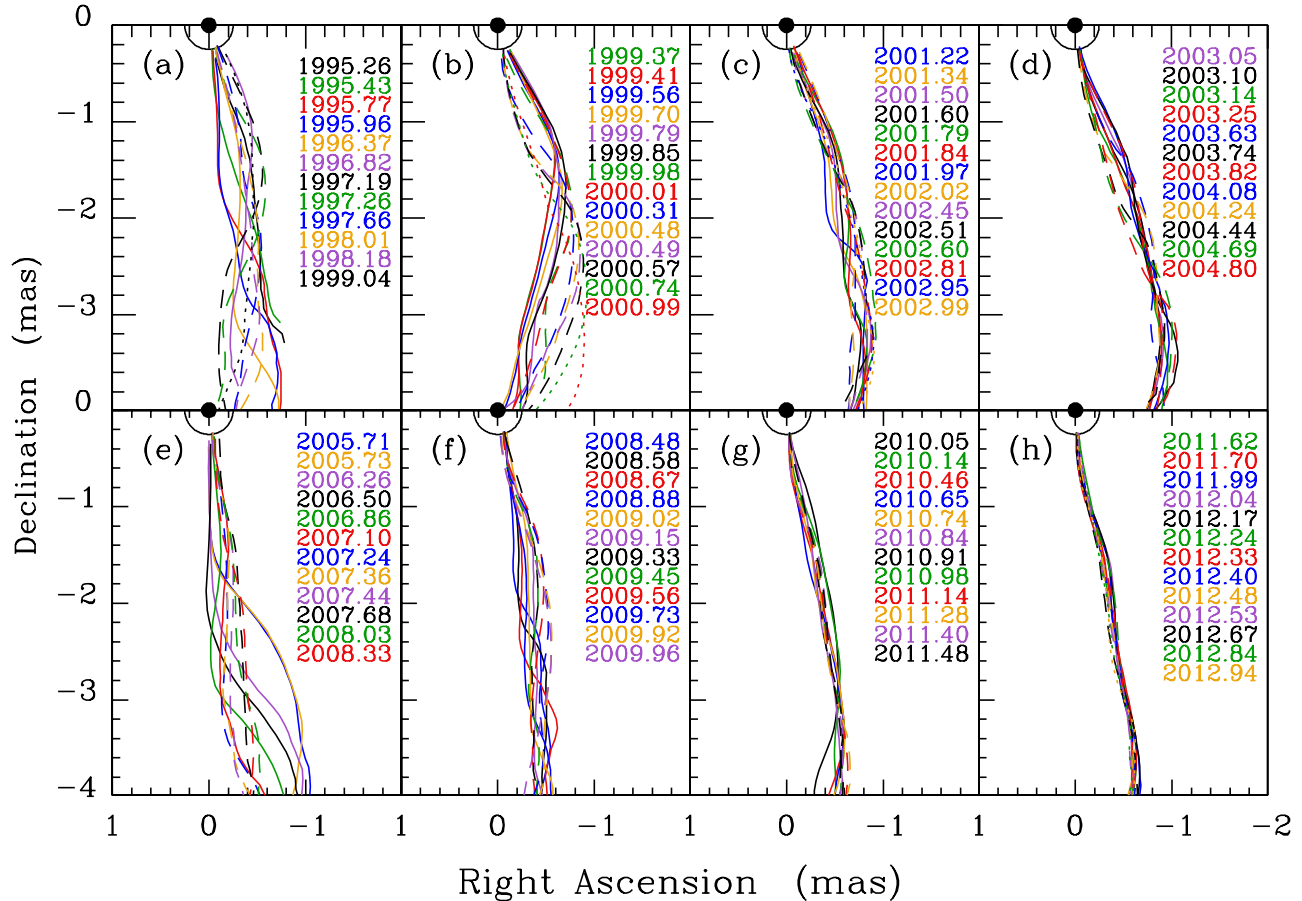


Figure 2. Ridge lines for BL Lac, 1995.26 – 2012.94. Successive panels are adjacent in time except that there is a 1-year gap between panels (d) and (e). Epochs are identified by color. In each panel the first occurrence of a color is further identified as the solid line, the next occurrence as a dashed line, and the third occurrence, when it exists, as a dotted line.

a jet is considered in Section 3, and the transverse waves and their velocities, including the behavioral change in 2010, are presented and discussed in Section 4. Excitation of the waves by changes in the P.A. of the RCS is considered in Section 5. In Section 6 we identify the waves as Alfvén waves, discuss their properties, and present some simple models of the system.

For BL Lac $z = 0.0686$, and the linear scale is 1.29 pc mas^{-1} . An apparent speed of 1 mas yr^{-1} corresponds to $\beta_{\text{app}} = 4.20$.

2. OBSERVATIONS

For this study of BL Lac we use 114 epochs of high-resolution observations made with the VLBA at 15 GHz, between 1995.27 and 2012.98. Most of the observations (75/114) were made under the MOJAVE program (Lister & Homan 2005), a few were taken from our earlier 2-cm program on the VLBA (Kellermann et al. 1998), and the rest were taken from the VLBA archive.

The data were all reduced by the MOJAVE team, using standard calibration programs (Lister et al 2009). Following the reduction to fringe visibilities we calculated three main products at nearly every epoch: (1) an image, consisting of a large number of “clean components” derived from the visibility function. The images in Figure 1 consist of the clean components convolved with a “median restoring beam”, defined in Section 3. (2) a model consisting of a small number of Gaussian “components” found by model-fitting in the visibility plane; each component has a centroid, an ellipticity, a

size (FWHM), and a flux density. The Gaussians are circular when possible. The centroids of the components for each epoch are plotted on the images in Figure 1. (3) the ridge line, shown in Figure 1 and discussed in Section 3. The image, the components, and the ridge line are not independent, but each is advantageous when discussing different aspects of the source. In most cases the ridge line runs down the smallest gradient from the peak of the image, and the components lie on the ridge line. However, when the jet has a sharp bend the algorithm can fail, as in Figure 1c. This is discussed in Section 3.

The components are assumed to represent regions of excess brightness that persist across epochs, and are not merely items in a mathematical list that sums to the measured image; see Paper I, also e.g., Lister et al (2009). We attempt to observe BL Lac frequently, every three or four weeks, to ensure that the components can be tracked unambiguously from epoch to epoch. In this paper we only use components that have been reliably measured four or more times, and have flux density $> 20 \text{ mJy}$.

The centroid locations are measured relative to the core, which we take to be the bright spot at the north end of the source; it usually is regarded as the optically-thick ($\tau = 1$) region of the jet. In principle, the core can move on the sky. We considered this in Paper I, and concluded that any motions are less than $10 \mu\text{as}$ in a few years, and they were ignored. Our positional accuracy is conservatively estimated as $\pm 0.1 \text{ mas}$, and in this paper we again ignore any possible core motions.

The components move in a roughly radial direction, and plots of $r(t)$ as well as the sky (RA–Dec) tracks are shown in Paper I and in Lister et al (2013). The tracks cluster around an axis at P.A. = -166° and appear to emanate from a strong quasi-stationary component, C7, that we identified as an RCS in Paper I. The moving components have superluminal speeds; the fastest has $\beta_{\text{app}} = 10 \pm 1$ in units of the speed of light. (Lister et al 2013)

3. THE RIDGE LINES

We are dealing with moving patterns on the jet of BL Lac, and in order to quantify them we first need to define the ridge line of a jet. At least four definitions have been used previously. Britzen et al. (2010b) used the line that connects the components at a single epoch, in studying 1803+784. Perucho et al (2012) investigated three methods of finding the ridge line: at each radius making a transverse Gaussian fit and connecting the maxima of the fits, using the geometrical center, and using the line of maximum emission. They found no significant differences among these procedures, for the case they studied, 0836+710. They showed that the intensity ridge line is a robust structure, and that it corresponds to the pressure maximum in the jet.

To quantify a ridge line we start with the image as in Figure 1, which is the convolution of the “clean components” with a smoothing beam. Since we are comparing ridge lines from different epochs, we have used a constant “median beam” for smoothing, and not the individual (“native”) smoothing beams. The latter vary a little according to the observing circumstances for each epoch, and their use would effectively introduce “instrumental errors” into the ridge lines. The median beam is a Gaussian with major axis = 0.89 mas (FWHM), minor axis = 0.56 mas and P.A. = -8° . Each of the three parameters is the median of the corresponding parameters for all the epochs.

The algorithm for the ridge line starts at the core, and at successive steps (0.1 mas) down the image finds the midpoint, where the integral of the intensity across the jet, along a circular arc centered on the core, is equal on the two sides of the arc. The successive midpoints are then smoothed with a third-order spline.

Ridge lines are shown on the three images in Figure 1. In Figure 1a the bends in the jet are gradual and the algorithm works very well, as indeed would any of the methods mentioned above. In Figure 1b there are two sharp bends and our algorithm makes a smooth line that misses the corners of the bends. In this case connecting the components would be better, if the modelling procedure actually put a component at the corner. In Figure 1c the jet appears to bifurcate, and our algorithm picks the west track. In this case a visual inspection of the image is required to see what is going on.

In fact there is another problem with Figure 1c. The image has a step to the east (looking downstream) about 1 mas from the core, where a short EW section connects two longer NS sections. Since the restoring beam is nearly NS the details of this step cannot be reconstructed. The calculated ridge line in Figure 1c does not reproduce the step, but makes a smooth track.

Figure 2 shows nearly all the ridge lines that we consider in this paper; a few are not shown because they occur very close in time to another one. The epochs are identified by color, and are further identified by the line type: in each panel the first occurrence of a color is shown solid, the second is shown dashed, and the third, when it exists, is shown dotted.

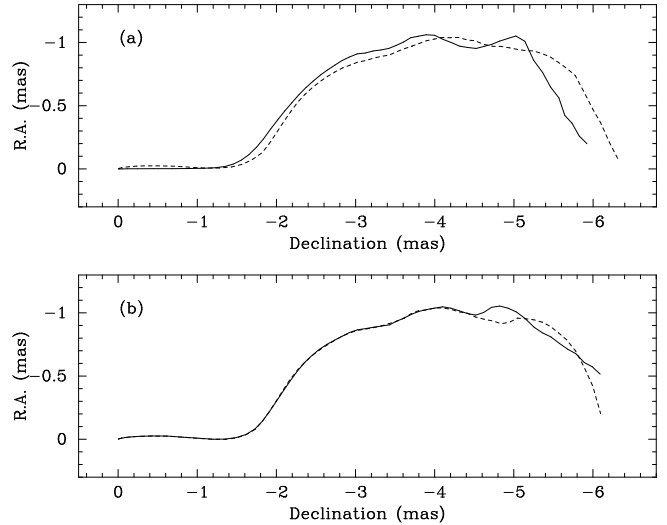


Figure 3. Ridge line for 2005–09–16 calculated (a) with native beams and (b) with median beam. Solid line: using all the antennas, dotted line: omitting SC and HN. In (a) the beam P.A.s differ by 17° .

The core is shown as the solid dot at the origin of each panel, and the semi-circle is drawn at $r = 0.25$ mas as a convenience. The RCS is located close to the circle, but is not shown in the figures. All the ridge lines are drawn relative to the core.

It is important to establish the reliability of the ridge lines because our analysis rests on them, and some of the structures that we interpret as waves are smaller than the synthesized VLBA beam. We first note that as with all VLBI our sampling of the (u, v) plane is sparse, and different samplings can produce different ridge lines. To see how strong this effect is, we emulated an observation with missing antennas by analyzing a data set with and without one and two antennas, and we did this analysis both with the native restoring beams and the median restoring beam described above. The results for 2005-09-16 are shown in Figure 3; they are similar to the results we obtained for two other epochs. In Figure 3a we show two ridge lines, the solid one is calculated with the full data set and the dashed line is obtained when data from the SC and HN antennas are not used. The latter calculation does not use many of the baselines, including the longest ones. The chief effect is a shift of the pattern downstream, by roughly 0.1 mas. This shift is not a statistical effect, but is mainly due to the different smoothing beams that were used for the two cases. We found that the differences in the ridge lines increased with increasing difference in the P.A.s of the smoothing beams. In Figure 3a the difference in P.A. of the smoothing beams is 17° .

In Figure 3b we used the median beam. In this case the curves are close with differences of typically $3 \mu\text{mas}$ out to 4 mas, where the surface brightness becomes low. Beyond 4 mas the differences rise to $50 \mu\text{mas}$.

Another way to investigate the reliability of the ridge lines is to examine pairs of ridge lines measured independently but close together in time. The full data set contains 10 pairs where the separation is no more than 10 days, and these are all shown in Figure 4. They are calculated with the median restoring beam. Note that the bottom three panels have a different vertical scale than the others. In general the comparison is very good within 4 mas of the core. Panel (i) contains one ridge line that stops at -3.6 mas because the brightness at the ridge becomes too low; this limit also can be seen in a few places in the other figures. Panel (i) contains the

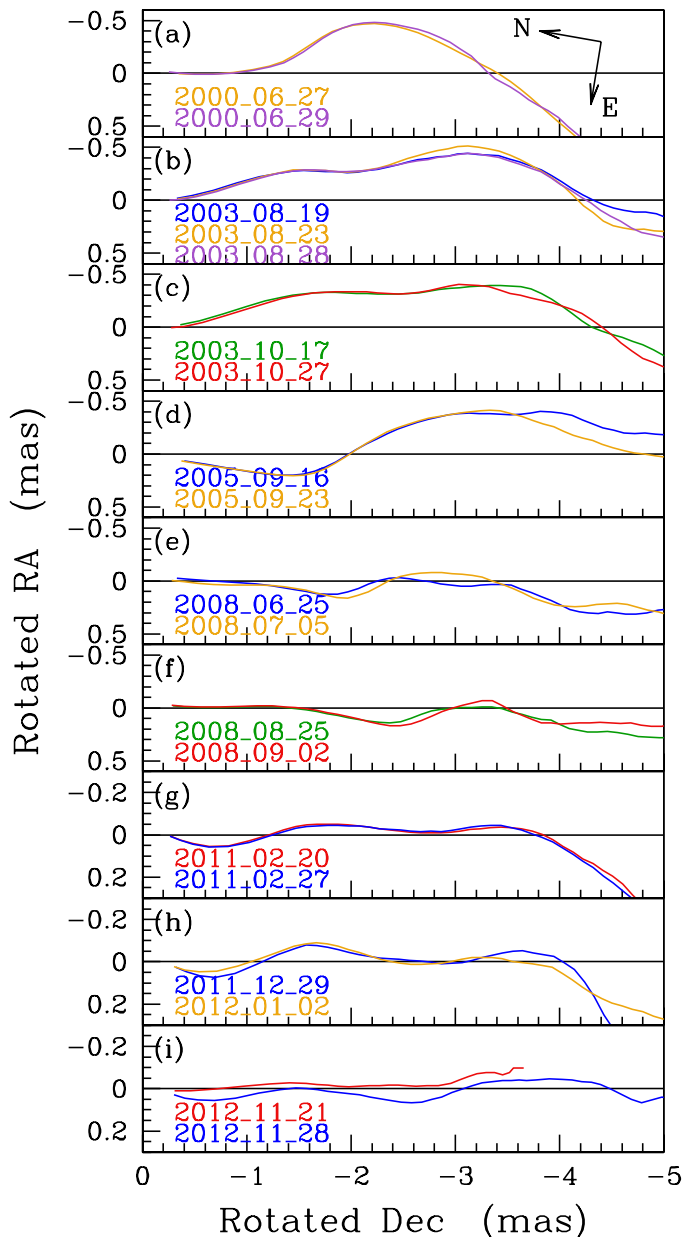


Figure 4. Ridge lines for 10 close pairs. The axes are rotated from (RA, Dec) by 9.5° ; North and East are indicated at top. The bottom 3 panels have a different vertical scale than the others, and the coordinate directions are thereby changed by a small amount.

only pair that has a continuous offset, of about $30\text{--}50\ \mu\text{as}$. These data were taken during an exceptional flux outburst at 15 GHz in BL Lac, seen in the MOJAVE data (unpublished), and roughly coincident with outbursts seen at shorter wavelengths (Raiteri et al. 2013). An extra coreshift leading to a position offset is expected with such an event (Kovalev et al. 2008). In any event, this pair appears to be different from the others, and we do not include it in the statistics.

Figure 5 shows the histogram of separations between the paired ridge lines, after excluding those in panel (i) of Figure 4. In forming the ridge lines a 3-pixel smoothing was used, and for the histogram we have used every third point. The median separation is $13\ \mu\text{as}$. Thus the repeatability of the ridge lines is accurate to about $13\ \mu\text{as}$. The reliability also depends on the effect discussed in connection with Figure 1,

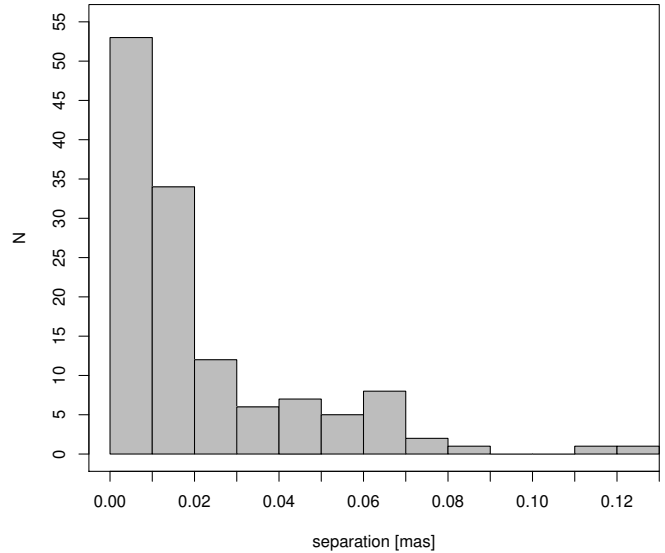


Figure 5. Histogram of separations between members of 9 close pairs of ridge lines. The pairs are shown in Figure 4 but panel (i) is not included in the histogram. See text.

that the ridge-finding algorithm can smooth around a corner, and can be in error by perhaps $100\ \mu\text{as}$. However, the error is roughly constant over short time spans, as in Figure 4 panel (e) where the sharp bend at $\sim 1.5\ \text{mas}$ is smoothed the same in the two curves. This smoothing will have little effect on calculations of wave velocity, which is the main quantitative use of the ridge lines. We ignore the smoothing in this paper.

From this investigation we conclude that caution must be taken in interpreting the ridge lines, especially when comparing ridge lines obtained at different epochs. The details of the restoring beam can have a noticeable effect on the ridge line, and to avoid misinterpretation the restoring beam should be the same for all the ridge lines that are being intercompared.

When considering these ridge lines it is important to keep the geometry in mind: the jet has a small angle to the line-of-sight (LOS), and the foreshortening is about factor of 10 (Paper I). Also, the projected images in Figure 1 can hide three-dimensional motions. To work with skew and non-planar disturbances, we use the coordinate systems shown in Figure 6. East, North, and the LOS form the left-hand system (x, y, z) and the jet lies at angle θ from the LOS in the *sagittal plane*¹³ formed by the LOS and the mean jet axis. This plane is perpendicular to the sky plane and is at angle P.A. from the y axis. The rotated system (ξ, η, ζ) is used to describe transverse motions: ξ is in the sagittal plane, η is perpendicular to it, and ζ is along the jet. By “transverse motion” we mean that a point on the beam has a motion in the (ξ, η) plane: v_ξ, v_η . The component v_ξ lies in the sagittal plane and its projection on the sky is along the projection of the jet. The ξ component of the transverse motion therefore is not visible, although a bright superluminal feature moving in the ξ direction would be seen as moving slowly along the jet. However, the v_η component remains perpendicular to the LOS as θ or P.A. changes, and its full magnitude is always seen. Thus a measured transverse motion is a lower limit. If the beam is relativistic then time compression of the forward motion must be added; see Section 4.3.

¹³ The term is taken from anatomy, where it refers to the plane that bisects the frontal view of a figure with bilateral symmetry. It is also used in optics, in discussions of astigmatism.

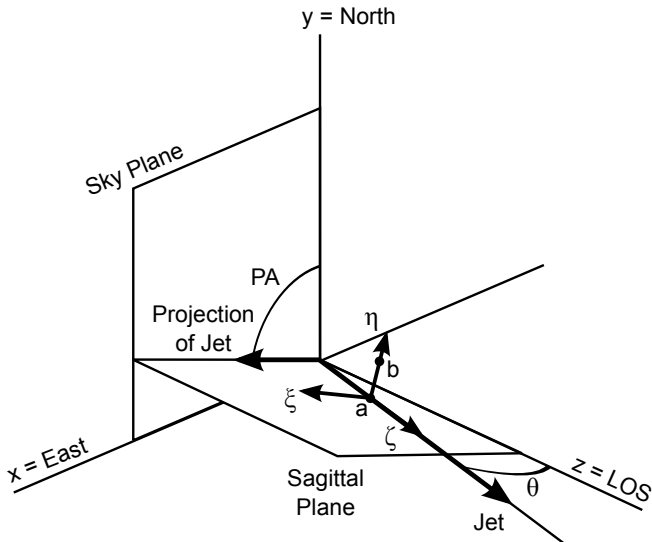


Figure 6. Coordinate system. The sagittal plane is defined as the plane containing the LOS and the mean jet axis; see text.

Some of the panels in Figure 2 show disturbances that appear to move down the jet, and at other epochs the jet is fairly quiet. We now consider several of the disturbances in detail, starting with the structures seen in Figure 2, panel (b).

4. WAVES ON THE RIDGE LINES

Figure 7 is an expanded view of Figure 2, panel (b). It includes ridge lines for 14 consecutive epochs over a period of about 1.6 yr. Beyond 1 mas the early epochs (solid lines) show the jet bending to the SE. Later epochs show the bend farther downstream, and at 2000.31 and later the jet bends to the SW before bending SE. We anticipate a result from Section 4.2 and draw vector A at P.A. = -167° across the tracks. The intersections of vector A with the tracks are shown in the inset in Figure 7. The velocity implied by the line in the inset is close to 1 mas yr^{-1} or $\beta_{\text{app}} \approx 4.2$. The pattern on the ridge line is moving downstream at nearly constant velocity. We consider three possible explanations for this.

1) We see the projection of a conical pattern due to a ballistic flow from a swinging nozzle, like water from a hose. The argument against this is that line B in Figure 7 is parallel to vector A and approximately tangent to the western crest; this line is not radial from the core as it would be if it were a ballistic flow. In Figure 2 all the panels except (a), (b), and (e) show clearly that the flow is constrained to lie in a cylinder, not a cone.

2) The moving pattern is due to a helical kink instability that is advected downstream with the flow. In the kink the field is stretched out and becomes irregular and may no longer be dominated by the toroidal component (Nakamura & Meier 2004; Mizuno, Hardee, & Nishikawa 2014), especially when averaged over the VLBI resolution beam. This should reduce the fractional polarization substantially, and could produce an EVPA normal to the wave crest in Figure 7 rather than longitudinal. But in BL Lac the fractional polarization remains high and the field remains longitudinal, along the bend. In Figure 8 we show the polarization image for one of the epochs for the large wave shown later in Figure 10. Figure 8 is taken from the MOJAVE website¹²; see also O’Sullivan & Gabuzda (2009). In Figure 8 the linear polarization fraction p is indicated by the color bar, and in the right-hand figure tick marks show the EVPA corrected for the Galactic Faraday Rotation.

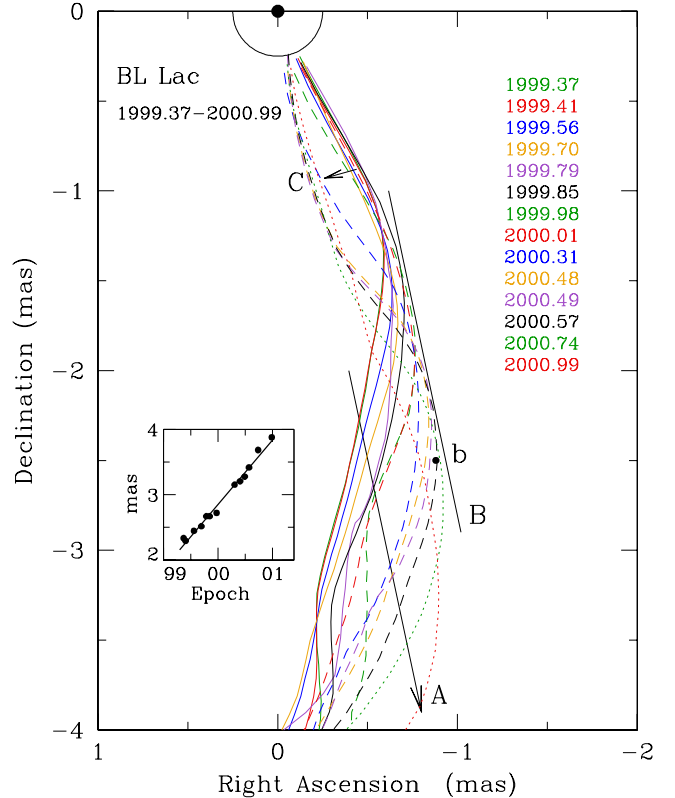


Figure 7. Ridge lines for BL Lac at 15 GHz, for 14 epochs between 1999.37 and 2000.99. Below Dec = -2 mas , the displacement in space corresponds to a displacement in time, and the inset shows the points where the vector A crosses the ridge lines – the ordinate is distance along the vector A. The velocity in the A direction is 0.92 mas yr^{-1} at P.A. = -167° ; the arrow itself represents the propagation vector that is derived in the text. The offset straight line B is parallel to the propagation vector. It is approximately tangent to the wave crests, and so the wave has constant amplitude as it moves to the SW. The short arrow C shows a swing of the jet from west to east in early 2000; see text Section 5. The point b shows the characteristic point on the 2000.57 line where the slope changes; see text Section 4.2. Colors are as in Figure 2.

The EVPA is nearly parallel to the jet out to about 5 mas, and p is high on the ridge, up to $\sim 30\%$ except near the core and in a slice at 2 mas where it drops to $p = 15\%$. This drop presumably is due to the blending of orthogonally polarized components at the bend in the jet, where the EVPA changes. We think it likely that the EVPA and fractional polarization data preclude the identification of the structures seen in Figure 7 as an advected kink instability.

3) The moving patterns are transverse MHD waves; i.e., Alfvén waves. For this to be possible the plasma must be dynamically dominated by a helical magnetic field. This condition for the jet of a BL Lac has been suggested many times, see e.g., Gabuzda, Murray & Cronin (2004), Meier (2013). Note that we implicitly assumed the helical, strong-field case in discussing the kink instability, in the preceding paragraph, and we also assumed it in Paper I. Thus, we assume that the moving pattern under vector A in Figure 7 is an Alfvén wave, with velocity $\sim 1 \text{ mas yr}^{-1}$.

In Figure 7 a second wave is seen between $r = 1$ and $r = 2$ mas, where the ridge lines for epochs 2000.31 and later bend to the SW. The two waves in Figure 7 can be thought of as one wave with a crest to the west. This wave is generated by a swing of the nozzle to the west followed by a swing back to the east about 2 years later, as discussed below in Section 5.

The 1999–2000 wave is displayed in a different form in Fig-

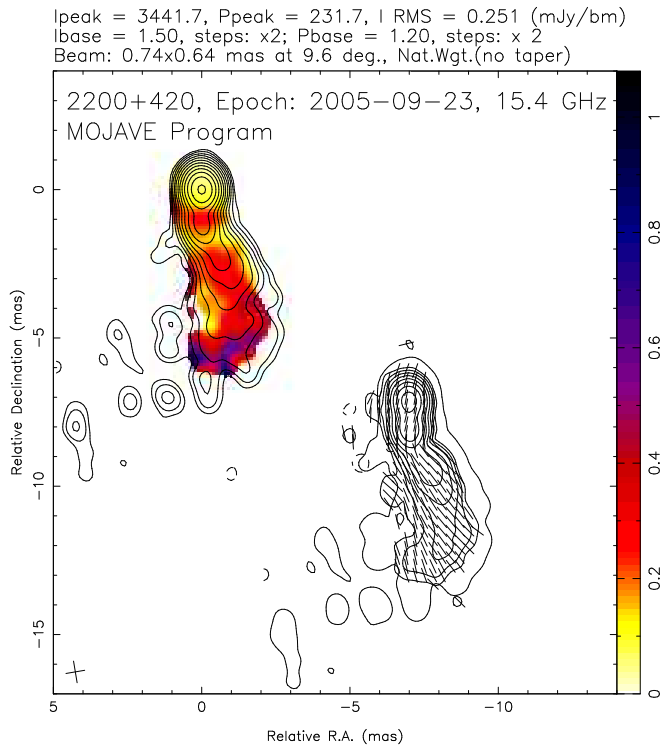


Figure 8. Polarization image for BL Lac epoch 2005-09-23, one of those forming the large wave in Figure 10. Linear polarization fraction p is indicated by the color bar; at the core $p \approx 6\%$, in the slice at ~ -2 mas p drops to 15%, and on the ridge p remains near 30% from 2 to 4 mas. In the right-hand image tick marks show the EVPA corrected for Galactic Faraday Rotation; the EVPA stays nearly parallel to the jet out to about 5 mas.

ure 9, which shows the ridge lines from 1999.37 to 2001.97. Vertical spacing is proportional to epoch, and the axes have been rotated by 13° ; arrows at top show North and East. Tick marks on the right are 0.1 mas apart. The dots show the points described later in Section 4.2, where the slope changes, and the solid line A is a linear fit through the points, with speed $v = 0.92 \pm 0.05 \text{ mas yr}^{-1}$. This wave is prominent until 2000.99. In 2001.22 the structure has changed. There are alternate possibilities to explain this new structure, B. It may be a new wave, with the crests connected with line B (drawn with the same slope as line A). In this case the wave must have been excited somehow far from the RCS. The fit of line B to the wave crests is poor and would be improved if acceleration were included, but there is not enough data for that. Alternatively, structure B may simply be a relic of the trailing side of wave A, perhaps relativistically boosted by the changing geometry (the bend) seen in Figure 2 panel (c). A third wave C is shown by the dashed line that again is drawn with the same slope.

Panel (c) of Figure 2 shows the ridge lines projected on the sky for 2001 – 2002. Wave B from Figure 9 is seen as the bump to the east at $r = 2$ mas, which moves downstream at succeeding epochs. The projected axis of the jet is curved at these epochs, and the possible acceleration noted above for wave B may simply be a relativistic effect inherent in the changing geometry.

Wave A in Figure 9 is barely visible in Figure 2 panel (a) as a gentle bump in 1999.04, so it is first apparent in early 1999 at a distance $r \sim 1$ mas from the core. This is reminiscent of the behavior of the components discussed in Paper I; Figure 3 of that paper shows that most of the components first become visible near $r = 1$ mas. Wave C also appears to start near $r \sim 1$

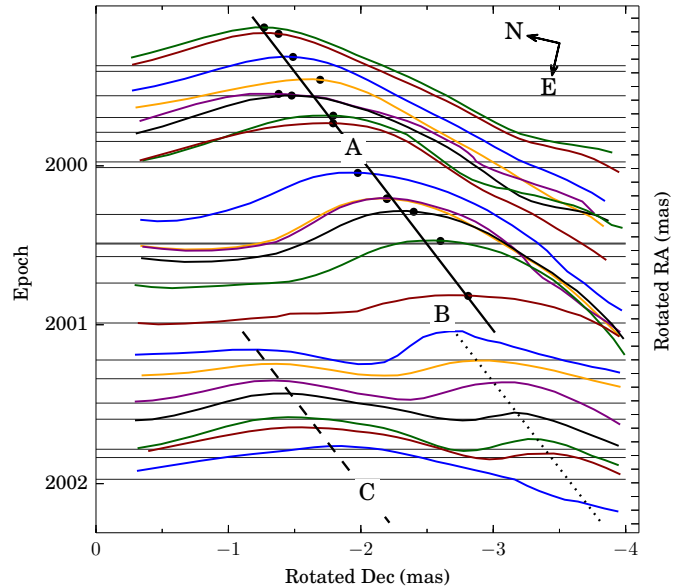


Figure 9. Ridge lines for 1999.37-2001.97, plotted on axes rotated by 13° . North and East are indicated at the top. The ridge lines are spaced vertically according to epoch, and the tick marks on the right-hand side are spaced 0.1 mas apart. The solid line is a linear fit to the dots, which are the characteristic points discussed in Section 4.2. The three lines are parallel and all have slope 0.92 mas yr^{-1} . See text.

mas.

In Figure 7 the short arrow C shows an eastward swing of the inner jet between 2000.01 and 2000.31. This is seen in Figure 9 in the ridge line for 2000.31, which shows a new inner P.A. The effect of these P.A. swings on the beam is discussed in Section 5.

The different panels in Figure 2 show that the jet can be bent, and even when relatively straight, can lie at different P.A.s. Hence there is no unique rotation angle for the ridge lines in a plot such as that in Figure 9. The rotation angle used in Figure 9 was found by the velocity algorithm described in Section 4.2 for wave A.

Further examples of waves are shown in Figures 10 – 12, omitting the extraneous ridge lines to avoid confusion. The wave motions are indicated by the arrows, which are propagation vectors derived in Section 4.2. Table 1 lists the details for these waves. μ is the measured proper motion, β_{app} is the apparent motion in units of c , $\beta_{\text{wave}}^{\text{gal}}$ the wave speed in the coordinate frame of the galaxy, assuming $\theta = 6^\circ$, P.A. is the direction of the propagation vector, and the amplitude is an estimate that is not well-defined but is an indication of the strength of the wave. The 2005 wave is the largest such feature seen in the data. Unfortunately, there was an 11-month data gap prior to 2005.71, and the wave cannot be seen at earlier times.

The amplitudes of the larger waves appear to be comparable with the length scale, as indicated for example by the length of the diagonal part of the wave in Figure 7. However, this is an illusion caused by the foreshortening. The angle to the LOS $\theta \approx 6^\circ$ and the foreshortening is approximately a factor of 10. (Paper I). The amplitude is therefore only a few percent of the length scale. The wavelength itself is not a well-defined quantity, as the system is not periodic, at least not on time scales up to 15 years. The length scales that we see in Figure 7 are controlled by the wobble in the nozzle at the RCS (see Section 5).

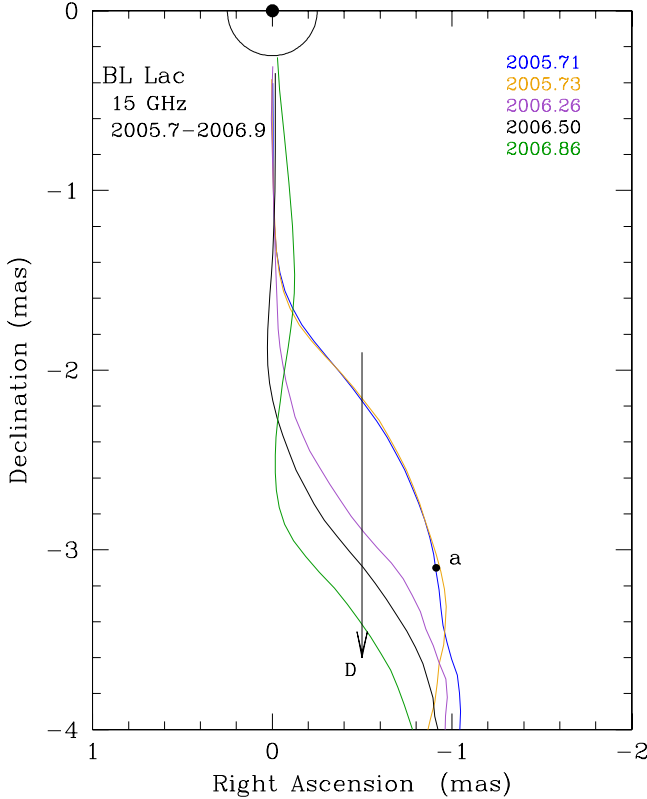


Figure 10. Ridge lines for BL Lac at 15 GHz, for 5 epochs between 2005.7 and 2006.9. The propagation vector for Wave D is at P.A. = -180° . Point a represents the advected beginning of the wave; see text.

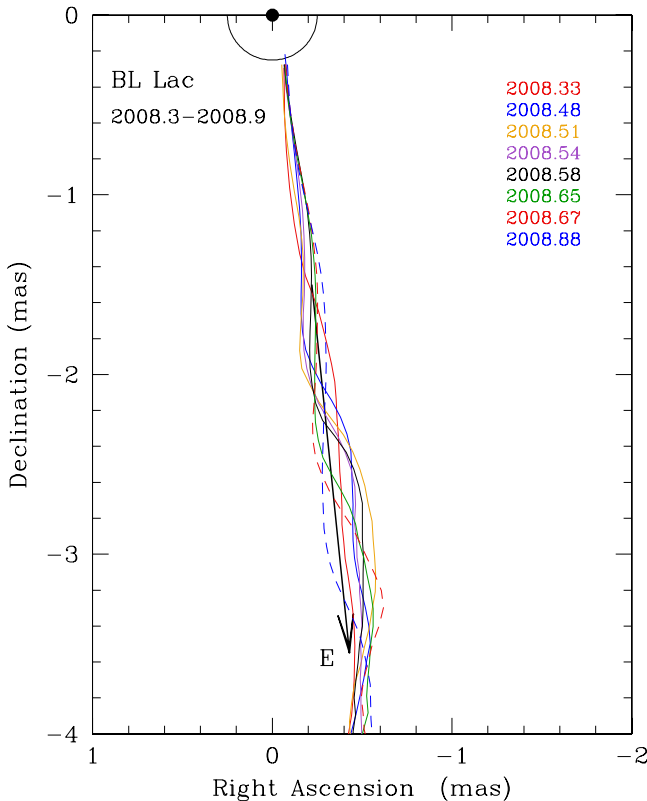


Figure 11. Ridge lines for BL Lac at 15 GHz, for 7 epochs between 2008.3 and 2008.9, showing Wave E with a propagation vector at P.A. = -175° .

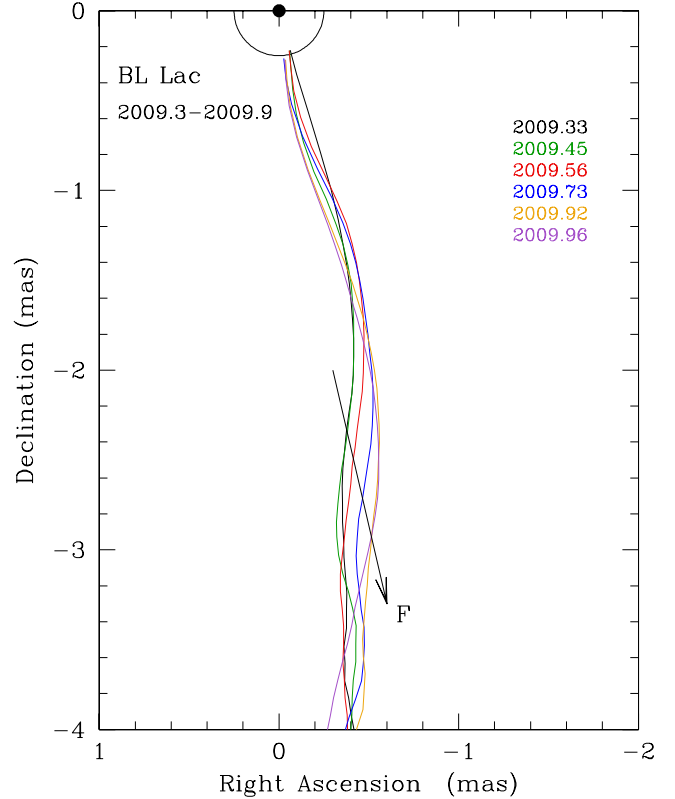


Figure 12. Ridge lines for BL Lac at 15 GHz, for 6 epochs between 2009.3 and 2009.9, showing Wave F with propagation vector at P.A. = -166° .

Figure 13 contains one frame of a movie of BL Lac showing the jet motions and ridge line fits at 15 GHz. The full movie is available in the electronic version of this paper or from the MOJAVE web¹⁴.

4.1. Different Jet Behavior in 2010-2013

In Figure 2 panels (g) and (h) we see that by 2010 the earlier activity in the jet has subsided, and that after 2010.5 the jet is well-aligned at P.A. = -170.5° with a weak wiggle. But the wiggle is not stationary. Figure 14 shows the ridge lines plotted on axes rotated by 9.5° , and spaced proportionately to epoch. Most of the ridge lines have a quasi-sinusoidal form, with the wavelength increasing down the jet, and the amplitude decreasing. Almost all the epochs show a negative peak in the inner jet, with a minimum near Dec = -0.7 mas. This is a quasi-standing feature, of variable amplitude. At most epochs there is a positive peak near Dec = -1.6 mas. This also is a quasi-standing feature, but less distinct than the inner one.

What is causing the quasi-standing features? The patterns can hardly be true standing waves because that requires a reflection region. A rotating helix would project as a traveling wave, as on a barber pole, so a simple barber-pole model is excluded. Possible motions of the core are only about $10 \mu\text{as}$ (Paper I), so any registration errors due to core motion are much smaller than the observed changes, which are up to $100 \mu\text{as}$. There is little indication of wave motion in Figure 14; at least, not at the speeds seen in Figure 2. Although the transverse Alfvén waves appear to have stopped during this period, the superluminal components, which we identified in Paper I as MHD acoustic waves, did not. Figure 2

¹⁴ <http://www.astro.purdue.edu/MOJAVE/bllacpaper2.mpg>

Table 1
Transverse Waves on the Jet of BL Lac.

Epoch	N	μ (mas yr ⁻¹)	$\beta_{app,T}$	β_{wave}^{gal}	P.A. (deg)	Amplitude (mas)	
A 1999.37-2000.99	14	0.92	±0.05	3.9	0.979	-167.0 ±1.4	0.5
D 2005.71-2006.86	5	1.25	±0.11	5.6	0.987	-180.2 ±1.1	0.9
E 2008.33-2008.88	8	3.01	±0.16	13.5	0.998	-174.2 ±0.7	0.3
F 2009.33-2009.96	6	1.11	±0.19	5.0	0.985	-167.1 ±2.4	0.2

Notes. Columns are as follows: (1) Wave label, (2) Inclusive range of epochs, (3) number of epochs, (4) apparent speed, (5) error, (6) apparent speed in units of c , (7) speed in galaxy frame, assuming $\theta = 6^\circ$, (8) P.A. of the wave, (9) error, (10) estimated amplitude.

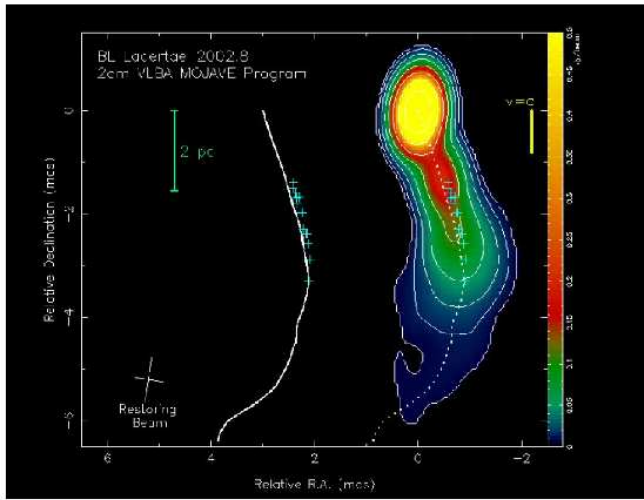


Figure 13. Movie of the BL Lac jet at 15 GHz. The total intensity image is on the right, with a color bar indicating flux density. The contour levels begin at 7 mJy per beam, and increase by logarithmic factors of 2. The false color scheme uses a square root transfer function, and is saturated at the core position in order to highlight changes in the much fainter jet. The core peak brightness is highly variable; typically it is between 2 and 6 Jy/beam. The projected linear scale is indicated by the 2 pc line at left. The movie frames are linearly interpolated between the individual VLBA epoch images, which have been registered to the fitted position of the core feature, and restored with a median beam with FWHM dimensions of 0.89×0.57 mas, with a major axis position angle at -8.6° , as indicated in the lower left corner of the frame. The fitted ridge line is shown as a dashed line in the image, and again as a solid line to the left of the image. These have also been linearly interpolated between the individual VLBA epochs. The points of changing slope (see Section 4.2) at individual VLBA epochs are shown as the small symbols. At left the ridge lines are shown with different colors for the various waves. The yellow $v = c$ line on the right is advancing at the speed of light ($\beta_{app} = 1$) and is included for reference.

in Paper I shows that they continued during this period, with about the same frequency and speed as earlier.

It appears then, that during the “quiet” period 2010-2013, the jet was essentially straight but with a set of weak quasi-stationary patterns, with variable amplitude. The superluminal components, however, continued as before. A further complication is that during the latter half of this period, from about 2011.4 to 2013.0, BL Lac was exceptionally active at shorter wavelengths (Raiteri et al. 2013), from 1 mm through gamma-rays. This behavior is not understood.

4.2. Velocity of the Waves

We estimated the velocity of Wave A in Figure 7 in two independent ways. In the first we assume that there is a constant propagation vector, and we shift and superpose the ridge lines on a grid of $(v, \text{P.A.})$ where v is the speed of the wave and P.A. is its propagation direction. If the ridge lines form a simple wave, then the solution is found when the lines lie on top of each other. This is shown in Figure 15, where a reasonable fit

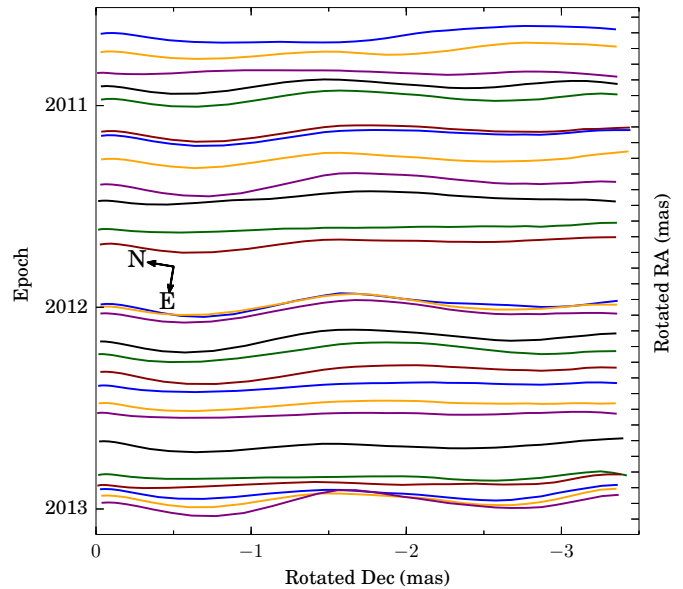


Figure 14. Ridge lines as in Figure 2 panels (g) and (h), plotted on axes rotated by 9.5° and with vertical spacing proportional to epoch. Tick marks on right-hand side are 0.1 mas apart.

can be selected by eye. The result is $v = 0.98 \pm 0.08$ mas yr⁻¹ at P.A. = $-168^\circ \pm 4^\circ$. This solution is somewhat subjective and the quoted errors do not have the usual statistical significance.

As an alternative procedure to visually aligning the ridge lines, we developed a method of identifying a characteristic point on the wave, just downstream of the crest, where the wave amplitude has begun to decrease. Define the slope of the ridge line as $\Delta x / \Delta y$ in pixels, where in Figure 9, x and y are rotated RA and Dec, and take the first downstream location where the slope exceeds ± 0.05 . This point is marked with the dot b on the ridge line for 2000.57 in Figure 7. The x and y positions vs time for these locations are then fit independently using the same methods as described in Lister et al (2009) to extract a vector proper motion for this characteristic point on the wave.

The two methods agree well and the analytic solution is $v = 0.92 \pm 0.05$ mas yr⁻¹ at P.A. = $-167.0^\circ \pm 0.5^\circ$, and the apparent speed is $\beta_{app} = 3.9 \pm 0.2$. The propagation vector is shown in Figure 7 and the speed and direction of the wave are listed in Table 1. The Table also includes β_{wave}^{gal} the speed of the wave in the galaxy frame, assuming $\theta = 6^\circ$. This calculation assumes that the ridge lines lie in a plane; i.e., are not twisted. This is not necessarily the case. Rather, since the inner jet, near the accretion disk, may wobble in 3 dimensions, (McKinney et al, 2013) it seems likely that the RCS will execute 3-dimensional motion and that the downstream jet will also. See Section 5.

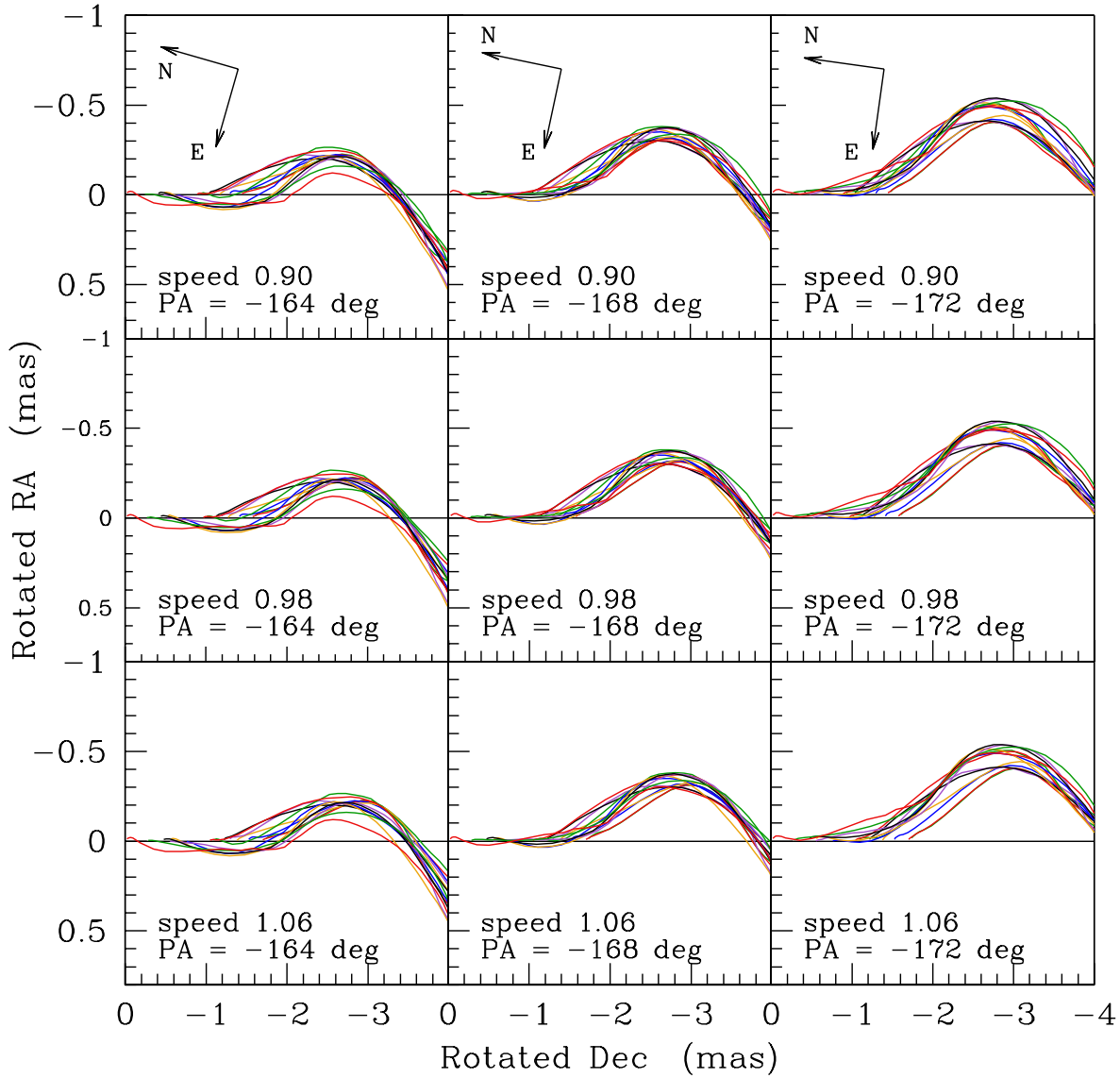


Figure 15. Ridge lines shifted and overlaid on a grid of propagation vectors, for the 14 epochs shown in Figure 7. Each panel shows the assumed P.A. and speed; the P.A. is constant in the columns and the speed is constant in the rows. The axes are rotated to bring the P.A. to horizontal; North and East are shown at the top. See text.

Note that the P.A. of the first and last propagation vectors in Table 1 ($-167^{\circ}0$, $-167^{\circ}1$) is the same (to within the uncertainties) as the P.A. of the axis ($-166^{\circ}6$) defined in Paper I as the line connecting the core with the mean position of the recollimation shock. In the context to be developed later, where the jet acts as a whip being shaken at the RCS, this close agreement is somewhat accidental. The shaking is rapid, and occurs about a mean direction. Tension in the whip continually pulls it towards the mean.

In Table 1 the speeds for the first, second and fourth waves are all similar at $\sim 1 \text{ mas yr}^{-1}$, but the 2008 wave is 3 times faster. The apparent speed for the 2008 wave is $\beta_{\text{app},2008} \approx 13.5$, which is comparable to the speed for the fastest component in BL Lac, $\beta_{\text{app}} \approx 10$, (Lister et al 2013). We defer further discussion of the 2008 wave to another paper.

4.3. Transverse Velocity

The ridge waves are relativistic transverse waves with apparent speeds β_{app} from 4.2 to 13.5 times the speed of light, and we assume that they have a small amplitude. From the

usual formula for apparent speed,

$$\beta_{\text{app},\text{wave}} = \frac{\beta_{\text{wave}}^{\text{gal}} \sin \theta}{1 - \beta_{\text{wave}}^{\text{gal}} \cos \theta} \quad (1)$$

and taking values of $\beta_{\text{app},T}$ from Table 1 and using $\theta = 6^{\circ}$, we find $\beta_{\text{wave}}^{\text{gal}} = 0.979 - 0.998$ for the speed of the waves in the frame of the host galaxy. We discuss the jet motion in terms of the coordinate system (ξ, η, ζ) shown in Figure 6. In response to the wave the jet has motion (v_{ξ}, v_{η}) . Component v_{ξ} lies in the sagittal plane and in projection lies along the projection of the jet. The ξ component of the transverse motion therefore is not visible, although associated intensity or polarization changes might be noticeable. However, v_{η} remains perpendicular to the LOS as θ or P.A. changes, and its full magnitude is always seen. Thus a measured transverse motion is a lower limit.

Consider a transverse motion that is in the (η, ζ) plane. Let the beam contain a co-moving beacon that is at the origin and emits a pulse at time $t' = 0$, where t' is in the coordinate frame

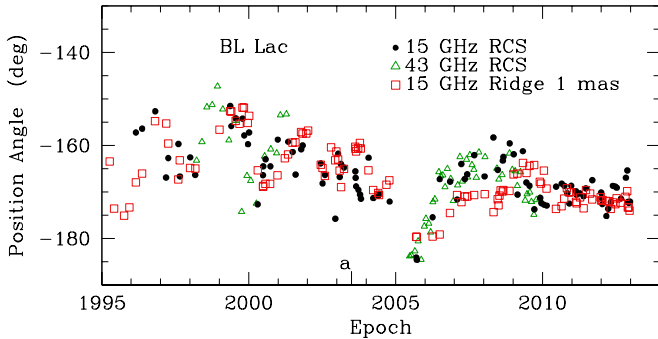


Figure 16. Position Angle versus Epoch for the RCS at 15 and 43 GHz, and for the Ridge Line at $r \approx 1$ mas. Epoch a represents the advected start of Wave D; see text.

of the galaxy. When $t' = 1$ yr the signal from the origin will have traveled 1 ly down the z axis, towards the observer. Also at $t' = 1$ the beacon has moved from the origin to the point $(\eta, \zeta) = (\beta_{tr}, \beta_{beam})$ where β_{tr} is the transverse speed, and β_{beam} is the longitudinal speed of the beam, both in the frame of the galaxy. At this point the beacon emits a second signal that also travels at the speed of light. In the z -direction, this signal trails the first one by $(1 - \beta_{beam}^{gal} \cos \theta)$ years. The apparent transverse speed of the beacon in the direction perpendicular to the jet, in the galaxy frame, is then

$$\beta_{app,tr} = \frac{\beta_{tr}}{(1 - \beta_{beam}^{gal} \cos \theta)} \quad (2)$$

$\beta_{app,tr}$ is to be differentiated from the apparent speed β_{app} commonly used in studies of superluminal motion, which is the apparent speed *along* the jet, projected on the sky. Note the close relation between Equations 1 and 2. Equation 2 can be inverted to find β_{tr} , a lower limit to the transverse speed.

For Wave A in Figure 7 we estimate a transverse speed at $r \sim 2$ mas by taking the transverse motion as 0.5 mas and the time interval as (2000.57 – 1999.41) yr, giving $\mu_{tr} \approx 0.43$ mas yr $^{-1}$ and $\beta_{app,tr} = 1.9$ and, from Equation 2 with $\theta = 6^\circ$ and $\Gamma_{jet} = 3.5$ (Paper I), $\beta_{tr}^{gal} \sim 0.09$. This is non-relativistic and consistent with our assumption that we are dealing with a low-amplitude wave.

5. EXCITATION OF THE WAVES

We suggested in Paper I that Component 7 is a recollimation shock, and that the fast components emanate from it. If this is correct, then the RCS should be a nozzle and its orientation should dictate the direction of the jet. In this Section we investigate this possibility. We first note that it is not possible to make a detailed mapping between the P.A. of the RCS and the later wave shape, for two reasons. First, the algorithm for the ridge line smooths over 3 pixels (0.3 mas), and thus smooths over any sharp features in the advected pattern. The second reason is more speculative. Our conjecture is that the wave is launched by plasma flowing through the nozzle and moving close to ballistically until its direction is changed by a swing in the P.A. of the nozzle. But tension in the jet continually pulls it towards the axis, and this means that it will bend, and that small-scale features will be stretched out and made smooth.

We start by comparing the P.A. of the RCS with the P.A. of the downstream ridge line at $r = 1$ mas. Figure 16 shows the P.A. of the RCS measured at 15 GHz and at 43 GHz. The latter is calculated from data kindly provided by the Boston

University VLBI group. We followed the conclusion found in Paper I, that the 15 GHz core is a blend of the first two 43 GHz components and that the 15 GHz component 7 is the RCS, as is the third 43 GHz component. We calculated the centroid of the first two 43 GHz components, to find an approximate position for the 15 GHz core, and then calculated the P.A. of the 43 GHz RCS from that centroid. The result is shown in Figure 16. We eliminated one discrepant point at 43 GHz, which was separated by about 20° from nearby 43 GHz points, and one discrepant point at 15 GHz. The correspondence between the two frequencies is generally good, especially after 2005.0 where the agreement is typically within 3° . This further justifies our claim (Paper I) that the the location of this component is independent of frequency, and that it is a recollimation shock.

Figure 16 also contains the P.A. of the 15 GHz ridge line, close to $r = 1.0$ mas. After 2005.0 the ridge P.A. lags the RCS P.A., by roughly 0.6 to 1.5 yr. After 2010 the P.A. of the RCS and the ridge line stabilizes and the variations, with rms amplitude about 3° , may mainly be noise. Prior to 2005.0 the variations are faster and stronger and the lag is erratic; in places there appears to be no lag but in 2003 it is about 0.5 y. It is clear, however, that the general character of the behavior of the ridge line is closely coupled to that of the RCS. When the RCS is swinging rapidly and strongly, as before 2005, then so also is the ridge at 1 mas, with little or no lag. When the RCS is swinging more slowly, then the ridge at 1 mas is also swinging slowly, and after 2010.0 they both are stable, with only small motions that may be dominated by measurement errors.

We conjecture that the large transverse waves on the ridge are excited by the swinging in P.A. of the RCS. Consider Wave A, seen in Figure 7. Its crest lies close to line B and moves downstream at 0.92 mas yr $^{-1}$. In 1999.37 the crest is at about $r = 1.2$ mas and at 0.92 mas yr $^{-1}$ would have been at the RCS ($r = 0.25$ mas) around 1998.3. This is in a data gap at 15 GHz, but at 43 GHz there was a peak in P.A. in mid- or late-1998. Given that in 1999 the time lag between the RCS and the ridge at 1 mas apparently was much less than 1 yr, the association between the peak in the RCS P.A. in 1998 and the crest of Wave A is plausible. The fall in P.A. in 1999 and 2000 is seen as the arrow C in Figure 7, and it corresponds to the upstream side of Wave A. The downstream side is the advected rise in P.A. of the RCS from mid-1997 to the peak in mid- or late 1998. The P.A. of the RCS fell from mid-1996 to mid-1997, and we might expect that there was a corresponding crest to the east on Wave A, about 1 mas downstream of the main crest to the west. In fact several of the earliest ridge lines in Figure 7 do show a minor crest to the east at about $r = 3.2$ mas, which is 2 mas, or 2 years at 0.92 mas yr $^{-1}$ downstream of the main crest to the west. A substantial acceleration in the wave speed would be needed for this to match. In any event, we cannot speculate usefully on this because it takes place beyond 3 mas, where there is a general bend to the east at all epochs. We conclude that a plausible association can be made between the large swing west then east of the RCS between 1998.0 and 2000.1, and Wave A that has a large crest to the west.

A similar connection can be made for Wave D, seen in Figure 10 in 2005–2006. It can plausibly be attributed to the large swing to the east of the RCS that started in 2003 or 2004 and continued into 2005. This wave does not have a crest as Wave A does, but a crude analysis can be made as follows. Assume

that point a on the 2005.71 ridge line is the advected beginning of the wave. With a speed of 1.25 mas y^{-1} (Table 1) this means that the swing to the east began around 2003.5. This date is shown as epoch a on the abscissa in Figure 16. Apart from one high point at 2004.1 the P.A. of the RCS falls gradually from 2003.1 until late 2004, when it must fall abruptly to meet the first point after the data gap in 2005. This also is seen in Figure 10; the first four epochs have ridge lines that lie together and are straight at P.A. $\approx -180^\circ$ out to $> 1 \text{ mas}$. This means that we can deduce the P.A. of the RCS from about 2004.7 to 2005.7: it was near -180° during that period. This is in a data gap, and this analysis suggests that the RCS P.A. was $\approx -180^\circ$ during most or all of the gap. Thus we can say that the large swing in P.A. of the RCS from mid-2003 until mid-2005 generated Wave D, the largest wave in our data set.

The P.A. of the RCS rose substantially from 2005.7 to about 2006.5, but there is no fast wave analogous to Wave D associated with it. The P.A. of the ridge does follow that of the RCS, as seen in Figure 16, but slowly; and in Figure 2, panels (e), (f) and (g), we see the ridge P.A. start at 180° and become curved, and slowly straighten out at $\sim -165^\circ$. This change is also a wave albeit a slow one.

As a further complication, during this slow straightening out of the jet we see two more low-amplitude waves. The high-speed Wave E (Figure 11) has no obvious antecedent in the P.A. of the RCS. Wave F (Figure 12) is seen a year after Wave E, at the “usual” speed of 1.1 mas y^{-1} . These waves together make a complex set of possibly twisted ridge lines, seen together in Figure 2 panel (f). We defer further discussion of these waves to another paper.

In Section 4.1 we showed that the waves on the jet subsided in 2010, and in 2010-2012 the ridge line had only a weak variable wiggle. During this time the P.A. of the RCS was essentially constant; the variations seen in Figure 16 may represent the errors in the measurements, which would be about $\pm 3^\circ$. These variations in space and time have some regularities, as discussed in Section 4.1, but they do not appear to have a connection to the P.A. of the RCS.

In Paper I we saw that the component tracks all appear to come from or go through the RCS (component 7) and that they lie in a window centered on P.A. $\approx -166^\circ$. This now is understood in terms of the waves on the ridge lines, since the components all lie on a ridge. The jet is analogous to a whip with a fixed mean axis being shaken with small amplitudes, in various transverse directions. The whip will occupy a narrow cylinder centered on the axis, and in projection the cylinder becomes our window.

6. ALFVÉN WAVES AND THE BL LAC WHIP

6.1. The Transverse Waves as Alfvén MHD Waves Along the Longitudinal Field Component

In Paper I we showed that the magnetic field in the jet of BL Lac has a strong transverse component. We assumed that it has a helical form, and that it is likely that the field dominates the dynamics in the jet. This is the condition for the existence of MHD waves that propagate down the jet. We suggested that the moving synchrotron-emitting components are compressions set up by fast and/or slow magnetosonic waves, possibly shocks. Now we introduce the third branch of MHD waves in the jet plasma, the Alfvén wave, which is a transverse S (shear) wave, with the disturbance occurring normal to the propagation direction. In Section 4 we showed that the moving patterns on the jet are transverse waves, and now we

suggest that they are Alfvén waves.

The phase speed of a transverse Alfvén wave is given by

$$\beta_T = \pm \beta_A \cos \chi \quad (3)$$

where $\beta_A = V_A/c$ is the relativistic scalar Alfvén speed, given in Equation A6 of Paper I, and χ is the angle between the propagation direction and the magnetic field. The Alfvén wave has similar propagation properties (with respect to the magnetic field direction) as the slow wave; i.e. it moves along the field, but not at all normal to it ($\cos \chi = 0$). Note that Alfvén waves generally will not produce shocks in an ideal MHD plasma.

6.2. Calculating Physical Quantities from the Wave Speeds

We now discuss these waves in the jet and present simple models that allow us to estimate the pitch angle α of the helix, which we define as the angle between the axis of the helix and the direction of the magnetic field when projected onto that axis.

A simple relation exists for the relativistic phase speeds of the three MHD waves:

$$\beta_s = \frac{\beta_F \beta_S}{\beta_T} \quad (4)$$

where β_s is the sound speed (relative to the speed of light), and β_F, β_S and β_T are the fast, slow, and transverse MHD wave speeds. Equation 4 may be readily verified from Equation 3 combined with Equations A1 and A2 of Paper I. With this result, the three equations for the phase speeds, together with the definitions of the cusp and magnetosonic speeds in Equations A3 and A4 in Paper I, can be solved for the magnetosonic and Alfvén speeds:

$$\beta_{ms}^2 = \beta_F^2 + \beta_S^2 - \beta_F^2 \beta_S^2 \quad (5)$$

$$\beta_A^2 = \frac{\beta_F^2 + \beta_S^2 - \beta_F^2 \beta_S^2 - \beta_s^2}{1 - \beta_s^2} \quad (6)$$

Finally, the propagation angle to the magnetic field χ can be found from Equations 3 and 6.

In dealing with this system of equations we are helped with constraints on the MHD wave speeds: $\beta_S < \beta_T < \beta_F < 1$, also $0 < \beta_s < 1/\sqrt{3}$ for an adiabatic sound wave in a relativistic gas. In addition, we adopt a constraint from the one-sidedness of BL Lac, $\Gamma_{jet} > 2.3$, where Γ_{jet} is the Lorentz factor of the beam in the frame of the galaxy; this gives a jet/counterjet intensity ratio of about 10^3 for $\theta = 6^\circ$ and a spectral index of -0.55 (Hovatta et al. 2014). We assume that the three waves travel downstream in the jet frame and parallel to the jet axis. Therefore, the propagation angle of all three waves is the pitch angle of the helix itself: $\chi = \alpha$.

We do not, in fact, measure the wave speeds themselves but rather their apparent speeds in the frame of the galaxy. To relate these to their speeds in the beam frame we first use Equation 1 and then the relativistic subtraction formula

$$\beta_{\text{wave}}^{\text{beam}} = \frac{\beta_{\text{wave}}^{\text{gal}} - \beta_{\text{beam}}^{\text{gal}}}{1 - \beta_{\text{wave}}^{\text{gal}} \beta_{\text{beam}}^{\text{gal}}} \quad (7)$$

where the superscripts define the coordinate frame.

We now have 5 input quantities to the calculation: $\beta_{\text{app},F}, \beta_{\text{app},S}, \beta_{\text{app},T}, \theta$ and Γ_{jet} , and with them we can calcu-

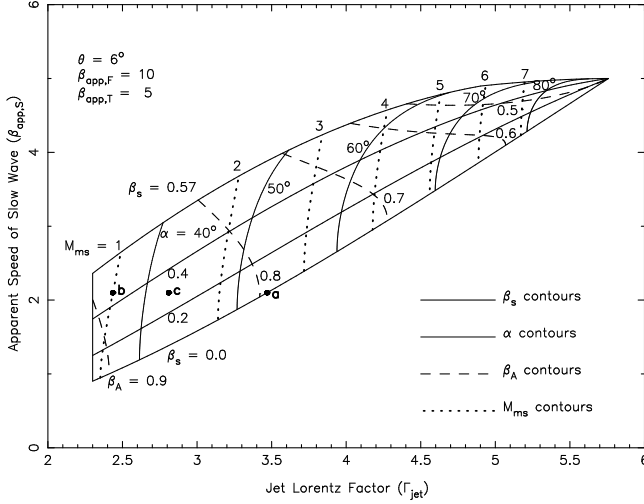


Figure 17. MHD waves along a relativistic beam containing a helical magnetic field. The two axes show quantities defined in the galaxy frame: jet Lorentz factor Γ_{jet} and the apparent (superluminal) speed of the slow wave $\beta_{\text{app},S}$ (the least-known of the three wave speeds). The interior of the diagram contains quantities defined in the beam frame: sound speed β_s (thick solid lines), Alfvén speed β_A (dashed), pitch angle of the magnetic helix α (thin solid line), and the magnetosonic Mach number M_{ms} (dotted). The region is bounded, approximately, by limits to the sound speed, 0 and $1/\sqrt{3}$, and by the limit to the Lorentz factor of the jet, $\Gamma_{\text{jet}} > 2.3$, set by the limit to the jet/counterjet ratio. The location of the diagram on the $\Gamma_{\text{jet}} - \beta_{\text{app},S}$ plane depends on the specific configuration of the other observer-related quantities shown at upper left. The three dots show the positions of the three models discussed in the text: (a) the cold plasma ($\beta_s = 0$) model, (b) the exactly trans-magnetosonic ($M_{ms} = 1$) model; and (c) the intermediate model.

late β_s , β_{ms} , β_A , α , and the magnetosonic Mach number defined as $M_{ms} = U_{\text{jet}}/U_{ms} = (\Gamma_{\text{jet}}\beta_{\text{jet}})/(\Gamma_{ms}\beta_{ms})$, where $U = \Gamma\beta$ is the magnitude of the spatial component of the four-velocity and $\Gamma = (1 - \beta^2)^{-1/2}$ is the Lorentz factor.

To illustrate the relationships among the various waves we show in Figure 17 (the banana diagram) the results for the specific configuration $\theta = 6^\circ$, $\beta_{\text{app},F} = 10$, $\beta_{\text{app},T} = 5$. These values correspond to the fastest superluminal component in BL Lac (Paper I) and to the apparent speeds of the transverse waves noted in Section 4 above. The diagram contains quantities defined in the frame of the beam: sound speed and Alfvén speed, α the pitch angle of the helix, and M_{ms} the magnetosonic Mach number. The diagram is bounded at the left and bottom by $\Gamma_{\text{jet}} = 2.3$ and $\beta_s = 0$. At the top, for $\alpha \lesssim 60^\circ$, the boundary traces the curve $\beta_s = 1/\sqrt{3}$, but for $\alpha \gtrsim 60^\circ$ (in this case), this curve sometimes ventures into a region where there are no solutions for α . This region can be eliminated from the banana by continuing the curve for $\alpha > 60^\circ$ with one that satisfies the criterion $d\alpha/d\Gamma_{\text{jet}} \approx 0$ at constant β_s , as we have done here. Inside the banana our conditions for magnetic dominance $\beta_A > \beta_s$ and $M_{ms} > 1$ are satisfied everywhere except in a thin quasi-horizontal region at top right, and in a thin quasi-vertical region at left. At the cusp $\alpha = 90^\circ$, indicating a purely toroidal field and no propagating Alfvén waves, regardless of the value of β_s . The banana diagram is set on the plane defined by the Lorentz factor of the jet and the apparent (superluminal) speed of the slow MHD wave, both measured in the galaxy frame. The location of the banana on this plane is set by the specific set of input parameters as on the top left.

6.3. Simple MHD Models of the BL Lac Jet

Figure 17 shows that knowing the apparent speeds of the three MHD waves and the angle θ of the jet to the line of sight is not enough to completely determine the jet properties. We must either determine one more quantity or make an assumption about the jet system. We will make three different assumptions for the sound speed, each yielding a simple model. The three cases are a cold jet, in which the plasma sound speed is negligible; an exactly trans-magnetosonic jet flow in which the jet plasma is near its maximum temperature; and a model intermediate between these two.

Model a: Slow-Mode Wave Speed is Negligible in Jet Frame. In Paper I we investigated a model of the jet in which an observed slowly moving component was due to a slow magnetosonic wave whose speed, relative to the jet plasma, was negligible (i.e., $\beta_s \approx 0$). In this case the apparent slow component speed is the beam speed itself. With this speed for the beam, we then assumed that a fast component was due to a fast magnetosonic wave, and, from the observed apparent speed, we were able to deduce its speed on the jet. This model can be placed in Figure 17. The model uses $\beta_s = 0$, $\theta = 6^\circ$, $\beta_{\text{app},F} = 10$ and $\beta_{\text{app},S} = 2.1$, and is located at the dot marked “a” on the boundary of the diagram at $\Gamma_{\text{jet}} = 3.47$, $\beta_{\text{app},S} = 2.1$. With $\Gamma_{\text{jet}}^{\text{gal}} = 3.47$ and $\Gamma_{\text{app},F}^{\text{gal}} = 10$, the fast pattern speed is three times greater than the speed of the beam, when the speeds are measured by their Lorentz factors. Because we now also have a measurement of the apparent transverse Alfvén wave propagation speed ($\beta_{\text{app},T} \approx 5$, a typical value from Table 1), we can extend this model to include computation of the total Alfvén speed β_A , the magnetosonic speed β_{ms} , and the magnetic field pitch angle α . With β_s^{beam} negligible, in the galaxy frame we again have $\beta_{\text{beam}}^{\text{gal}} = \beta_s^{\text{gal}} = 0.958$, $\beta_A^{\text{gal}} = \beta_F^{\text{gal}} = 0.995$, and now $\beta_T^{\text{gal}} = 0.985$. Then, using Equation 7, these become in the frame of the beam $\beta_s^{\text{beam}} = 0$, $\beta_A^{\text{beam}} = \beta_F^{\text{beam}} = 0.795$, and $\beta_T^{\text{beam}} = 0.478$, yielding $\alpha = \cos^{-1}(0.478/0.795) = 53^\circ$ – a moderate helical magnetic field. Since $\beta_{ms} = \beta_A$ when $\beta_s = 0$, we also can calculate the magnetosonic Mach number defined in Equation 5. This yields $M_{ms} = 2.5$ and qualifies this as a trans-magnetosonic jet. These numerical results for β_A , α , and M_{ms} are consistent with the dashed, solid, and dotted line contours in Figure 17.

Model b: Exact Trans-Magnetosonic Flow. In this case we derive the jet speed by assuming that the flow is *exactly* trans-magnetosonic; i.e. that the magnetosonic Mach number $M_{ms} = 1$. In Figure 17 the system sits at the intersection of the $\beta_{\text{app},S} = 2.1$ and the $M_{ms} = 1$ lines, shown by the dot “b”. This gives $\Gamma_{\text{jet}} \approx 2.4$ and $\alpha \approx 36^\circ$, a more open helix than in Model a. In this case $\beta_s \approx 0.45$ – near the maximum value of 0.577 and, yet, the pressure still is dominated by the magnetic field. This is a general consequence of models that avoid the upper-right ($\beta_A < 0.5$) part of the banana diagram.

Model c: An Intermediate Model. Our two models lie at extreme positions in the diagram in Figure 17 and neither seems plausible. For model a the plasma hardly can be cold because the source is a powerful synchrotron emitter and the electron temperature is probably of order 100 MeV; the electron component of the plasma therefore is probably relativistic. On the other hand, the sound speed may or may not be at 0.577c, depending on how heavily the plasma is contaminated with heavy, non-relativistic ions. Furthermore, for model b, the operating point is near the minimum jet Lorentz factor allowed by the jet/counterjet ratio. Hence, keeping

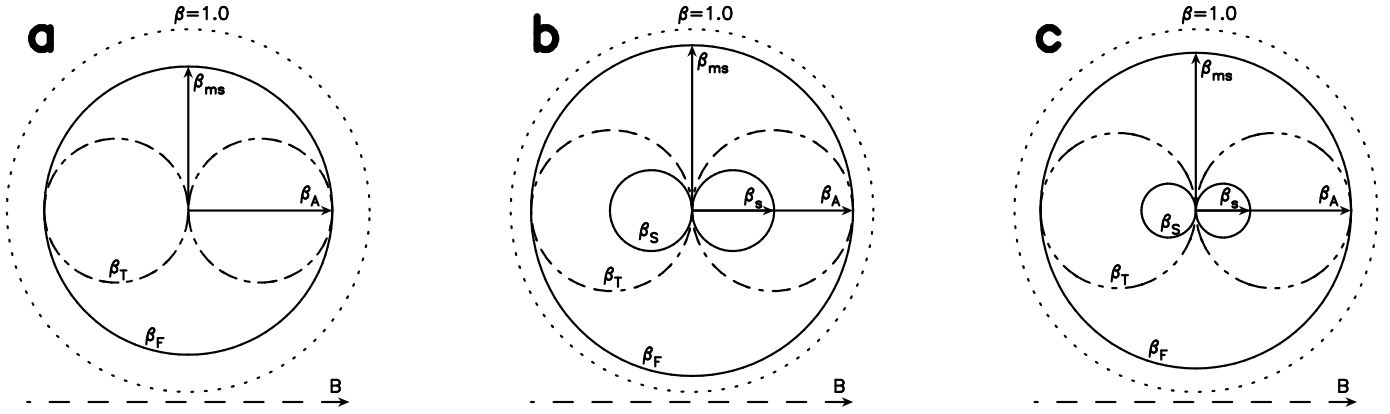


Figure 18. Relativistic phase polar diagrams for the three BL Lac jet models discussed in the text and identified in Figure 17. The diagrams show the wave speed at different angles to the magnetic field direction (dashed arrow) and are rotationally symmetric about the horizontal direction. (a) Model a (cold plasma): The slow branch does not appear because $\beta_s = 0$. In this model $\beta_A = \beta_{ms} = 0.794$, and the magnetic field pitch angle is $\alpha = 53^\circ$. Having the fastest jet Lorentz factor of the three models, it correspondingly has the slowest of the wave speeds that are consistent with the constraints in Figure 17. (b) Model b (exactly trans-magnetosonic): With $\beta_s = 0.453 \neq 0$ (close to the maximum sound speed), the slow branch now appears. Nevertheless, the magnetic field still dominates, with $\beta_A = 0.888$, $\beta_{ms} = 0.912$, and $\alpha = 36^\circ$. (c) Model c: This intermediate model has $\beta_s = 0.300$, $\beta_A = 0.857$, $\beta_{ms} = 0.870$, and $\alpha = 43^\circ$.

$\beta_{app,S} = 2.1$, but taking a moderately high value of $\beta_s \sim 0.3$, we obtain an intermediate model with $\Gamma_{jet} \sim 2.81$, $\alpha \sim 43^\circ$, $\beta_A \sim 0.857$, and $M_{ms} \sim 1.49$, indicated by the third dot in Figure 17. This describes a plasma in which the magnetic field is dominant but not overwhelming so, the field is in a moderate helix, and the jet flow is trans-magnetosonic. This is consistent with our original assumptions.

Therefore, the dominant helical field model for BL Lac implies a rather modest Lorentz factor for the actual plasma flow ($\Gamma_{jet} \sim 3$) and explains the faster propagation of the components and the transverse disturbances as MHD acoustic and Alfvén waves, respectively, in the jet frame. They are generated primarily at the site of the recollimation shock and propagate downstream on the helical field, each with a speed in the galaxy frame that is the relativistic sum of the wave speed in the jet frame and the jet flow speed in the galaxy frame.

Further insight into the propagation of an Alfvén wave on a jet can be gained by examining the group velocity, which has only one value, V_A , and is always directed along the magnetic field (Gurnett & Bhattacharjee 2005). An isolated wave packet will spiral down the jet along the helical magnetic field. A uniform disturbance across the jet will produce a ripple that moves along all the field lines; i.e. across the jet. The net result is a jump or bend that propagates downstream with speed proportional to the cosine of the pitch angle. This has a close analogy to a transverse mechanical wave on a coiled spring, or slinky. In both cases there is longitudinal tension, provided for the jet by the magnetic field.

6.4. Phase Polar Diagrams and the Internal Properties of the Jet Plasma

Figure 18 shows relativistic phase polar diagrams for the three models discussed above and identified in Figure 17. The diagrams show MHD wave phase speeds in 3-dimensional velocity space with the origin of each at the center of the diagram. Each diagram was computed using the relativistic equations A1-A6 in Paper I. All surfaces are axisymmetric about the horizontal magnetic axis. In each panel the dotted, solid, and broken lines show respectively the speed-of-light sphere (unity in all directions), the two compressional MHD wave surfaces (fast [β_F] and slow [β_S]), and the transverse Alfvén wave surface (β_T). Unlike the speed of light, the speeds of the MHD waves depend on the polar angle χ between the propagation and field directions. All three MHD modes are

labeled in the left half of the diagrams. The arrows labeled in the right half of the diagrams show the three characteristic wave speeds: sound (β_s), Alfvén (β_A), and magnetosonic (β_{ms}), which are realized only along the field for the slow and Alfvén modes and normal to the field for the fast mode. As mentioned earlier, the slow and Alfvén waves can propagate skew to the field, but not normal to it.

Some of the relationships among the three types of MHD waves can be seen in Figure 18b and c. The outer solid loop traces the fast magnetosonic mode, whose speed is a maximum β_{ms} at $\chi = 90^\circ$, and is the same as that of the Alfvén wave (dashed loop), β_A , when $\chi = 0^\circ$, provided $\beta_A > \beta_s$, where β_s is the sound speed in the plasma. The propagation speed of the Alfvén wave is proportional to $\cos \chi$ and this also is approximately true for the slow magnetosonic wave, the inner loop.

So far we have been discussing the propagation of Alfvén waves in a uniform magnetic field, and now address how this applies to a plasma jet with a helical field. Figure 19 shows a schematic diagram of a helical field jet with the properties of Model c discussed above and in Figures 17 and 18. The helical field will have a pitch angle of $\alpha = \chi \approx 43^\circ$, so the polar diagram in Figure 18 will be rotated by that amount. The propagation direction of the MHD waves points downstream in our model, allowing us to read off the values of their propagation speeds from the polar diagram: $\beta_S = 0.219$, $\beta_T = 0.631$, and $\beta_F = 0.863$. If the helical field and plasma properties are uniform along the jet, the results will be the same everywhere, producing MHD waves, each with a uniform velocity.

However, there will be a longitudinal current that will cause the field strength and pitch angle to be functions of the radial coordinate ϖ . (See the cut-away view of a plasma rope in Figure 6.14 of Gurnett & Bhattacharjee (2005), for a simple view of the radial variations in B and α .) But, there should be a cylindrical shell around the axis, covering a modest range of ϖ , in which the synchrotron emissivity into the direction of the observer is maximized. We assume that this shell is the dominant region and that the field strength and pitch angle there are the effective values that control the dynamics. So, if this is the case, then our dynamical analysis of the waves and a polarization analysis of the emission should result in similar magnetic pitch angle estimates for the magnetic field. However, preliminary polarization analysis (using methods similar

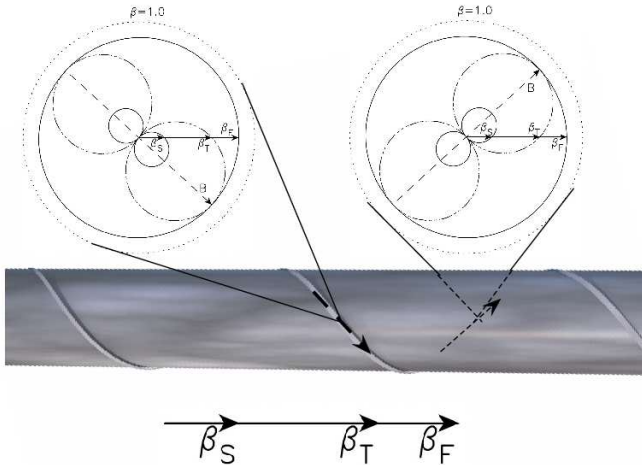


Figure 19. Role of the phase polar diagram in a helical magnetic field jet model. We show a relativistic plasma jet (medium grey flow) in its rest frame, described by model c (discussed in the text), and wrapped with one of its many helical magnetic field lines. At left the phase polar diagram in Figure 18c is rotated by the angle $-\alpha$ to align the dashed arrow with the helical field direction on the near side of the jet (left). The propagation speeds of the three MHD waves along the jet axis then can be directly read off the polar diagram ($\beta_S = 0.219$, $\beta_T = 0.631$, $\beta_F = 0.863$). For a uniform helical field one obtains the same results at any point (e.g., on the far side of the jet at right.)

to those in Murphy, Cawthorne & Gabuzda (2013) and discussed in more detail in the next paper in this series) produces estimates of 60° – 70° for the pitch angle, compared with the 36° – 53° range in the present paper. From Figure 17, then, one might expect higher jet Lorentz factors (4–5) and faster slow wave apparent speeds (3–4.5) than are in our model. While there are components in Paper I’s Figure 2 with such apparent speeds, there also are slower ones. One possible explanation, then, may be that the $\beta_{\text{app}} = 2.1$ wave that we chose in Paper I as our forward-propagating slow wave in fact is a *reverse* slow or fast wave, propagating upstream in the frame of the jet.

Furthermore, there are other possible explanations for the higher emission polarization pitch angles that are still consistent with our general model in this paper. It is quite possible that, because the azimuthal field B_ϕ will have structure, both radially and longitudinally, the wave dynamics may sample a region different from that sampled by the emission. *Radially*, for example, the field will have a peak $B_{\phi, \text{max}}$ at some ϖ_{max} (see, e.g., Lind et al. 1989) where the emission would be maximized. The wave dynamics, on the other hand, may sample a broader, more average, range of $B_\phi(\varpi)$ values, yielding lower values for the derived average pitch angle. Furthermore, there also will be *longitudinal* variations in B_ϕ when shocks are involved. In Figure 2 of Nakamura & Meier (2014), which does a 1.5-D numerical MHD simulation of the post-recollimation shock jet of M87, most of the jet that would control the dynamics of wave propagation has a pitch angle of $\sim 45^\circ$ in its rest frame. However, at the jet front, between the forward-fast and forward-slow shocks, where the emission due to accelerated particles is expected to be strong, the pitch angle rises to $\sim 60^\circ$, due to compression. Hence the radio polarization might indicate a pitch angle substantially larger than the dynamical wave analysis.

Our models for the jet have produced values for the Lorentz factor $\Gamma_{\text{jet}} \sim 2.5$ – 3.5 . This provides more than a factor of 10^3 for the jet/counterjet ratio of flux densities, which we took as a constraint. But $\Gamma_{\text{jet}} \sim 3$ is below previous estimates

of the Lorentz factor. Studies involving relativistic beaming and variability typically give $\Gamma_{\text{jet}} \sim 8$ – 11 (Jorstad et al. 2005; Hovatta et al. 2009) for BL Lac, but they fundamentally measure the Doppler boosting factor δ and not the Lorentz factor itself. The apparent speed β_{app} of a moving component is usually used as the speed of the beam, in calculating Γ from δ , but if the beam and pattern speeds are allowed to differ by an arbitrary amount, then one only has a limit: $\Gamma > \delta/2$. Thus, from Hovatta et al. (2009) we have $\Gamma > 3.6$, and from Jorstad et al. (2005) we also have $\Gamma > 3.6$. However, from a statistical point of view, such a small value for Γ is unlikely, because it requires $\theta \approx 0^\circ$; and values near $\Gamma \sim \delta$ are more probable. We conclude that beaming studies do suggest a value for Lorentz factor that is greater than we find in our dynamical models. This is related to the discussion in the previous two paragraphs, that the polarization of the synchrotron radiation suggests a tighter helix than we get with the dynamical analysis. It is likely that there is a common solution to both problems.

7. SUMMARY AND CONCLUSIONS

The jet of BL Lac is highly variable and displays transverse patterns that propagate superluminally downstream on the ridge line. They are not ballistic, like water from a hose; but are constrained, like waves on a whip. The magnetic field is well-ordered with a strong transverse component that we assume is the toroidal part of a helical field. In Paper I we assumed that the helical field provided support for fast- and slow-mode MHD waves whose compressions we see as the superluminal components. We here assume that the moving transverse patterns are Alfvén waves propagating on the longitudinal component of the magnetic field.

Six examples of the moving patterns are shown. Their durations range from 0.6 to 1.8 years, and their amplitudes from roughly 0.2 to 0.9 mas. A movie provides assistance in studying their motions.

The transverse wave activity died down in 2010 and the jet settled to a fixed position angle (P.A.), with a mild wiggle. This wiggle was not stationary, but appeared to oscillate transversely, with amplitude about 0.4 mas. This wiggle persisted through the remaining data period, up to 2013.0.

The velocity of the transverse waves was established by finding characteristic points on the ridge lines where the slope changes, as well as by visual inspection of the delayed superposition of the ridge lines. Three of the apparent velocities are near $\beta_{\text{app}} \approx 5$, and one is much faster, with $\beta_{\text{app}} \approx 13$. Taking the angle to the line-of-sight (LOS) $\theta = 6^\circ$ and Lorentz factor of the beam $\Gamma_{\text{beam}}^{\text{gal}} = 3.5$ gives speeds in the galaxy frame from $0.979c$ to $0.998c$.

The wave moves the jet transversely and the observed motion is converted into a transverse speed in the galaxy frame: $\beta_{\text{tr}}^{\text{gal}} \sim 0.09$. This is non-relativistic and consistent with our assumption that the waves have low amplitude.

The timing and direction of the waves is correlated with the P.A. of the recollimation shock (RCS), which swings over 25° in an irregular fashion. It appears that the waves are excited by the swinging of the RCS. This is analogous to exciting a wave on a whip by shaking it.

In Paper I (Figure 3) we saw that the ridge lines occupy a cylinder about 0.7 mas wide and 3 mas long, or 3 ly wide and 120 ly long when a deprojection factor of 10 is used. We now understand that this cylinder is formed by the transverse waves, whose axes generally are close to the source axis

at P.A. $\approx -166^\circ$. The width is set by the amplitude of the largest waves, while the length is set by the general bend of the source to the SE.

We briefly describe the Alfvén waves, and provide a method for calculating physical quantities in the jet in terms of the measured wave speeds. We investigate three simple models of the system; in the first the sound speed β_s is zero, the second is for exact trans-magnetosonic flow (magnetosonic Mach number $M_{ms} = 1$), and the third is for an intermediate case. The trans-magnetosonic model gives a value for the Lorentz factor of the jet of $\Gamma_{jet} = 2.4$, close to the limit set by the jet/counterjet ratio, and a moderate helix for the magnetic field, with pitch angle $\alpha \approx 36^\circ$. The intermediate model assumes that $\beta_s = 0.3$, and results in $\Gamma_{jet} \sim 2.8$, $\alpha \sim 43^\circ$, Alfvén speed $\beta_A \sim 0.86$, and $M_{ms} \sim 1.5$. This describes a plasma in which the magnetic field is dominant but not overwhelming so, and the field is in a moderate helix. While these results are broadly consistent with our original assumptions, our derived pitch angle is smaller than that expected from polarization studies. As discussed in Section 6.4, a pitch angle that changes with radius from the center-line of the jet, or a combination of higher Lorentz factors and higher wave speeds may naturally explain this difference. A probably related discrepancy with earlier results is that our model Lorentz factors are smaller than those derived from variability studies.

In our models the Lorentz factor for the jet is between 2.4 and 3.5, substantially smaller than the observed apparent speeds of the transverse waves. This is in agreement with the model result from Paper I, where the jet Lorentz factor was smaller than the apparent speed of the fast components. Hence, since the Lorentz factor of the pattern must be larger than the apparent speed of the pattern, the speed of the moving pattern must be the relativistic sum of the beam speed and that of a downstream wave on the beam.

We conclude that the rapid and strong transverse changes in the jet of BL Lac are manifestations of Alfvén waves excited at the RCS. The jet can be described as a relativistic, rapidly shaken whip. We suggest that other similar sources be investigated with these ideas in mind.

We are grateful to M. Perucho for reading the manuscript and offering helpful suggestions, and to the MOJAVE team for comments on the manuscript, and for years of work in producing the data base that makes this work possible. TGA acknowledges support by DFG project number Os 177/2-1. TH was partly supported by the Jenny and Antti Wihuri foundation and by the Academy of Finland project number 267324; TS was partly supported by the Academy of Finland project 274477. YYK is partly supported by the Russian Foundation for Basic Research (project 13-02-12103), Research Program OFN-17 of the Division of Physics, Russian Academy of Sciences, and the Dynasty Foundation. ABP was supported by the “Non-stationary processes in the Universe” Program of the Presidium of the Russian Academy of Sciences. The VLBA is a facility of the National Radio Astronomy Observatory, a facility of the National Science Foundation that is operated under cooperative agreement with Associated Universities, Inc. The MOJAVE program is supported under NASA-Fermi grant NNX12A087G. This study makes

use of 43 GHz VLBA data from the VLBA-BU Blazar Monitoring Program (VLBA-BU-BLAZAR¹⁵), funded by NASA through the Fermi Guest Investigator Program. Part of this research was carried out at the Jet Propulsion Laboratory, California Institute of Technology, under contract with the National Aeronautics and Space Administration. This research has made use of NASA’s Astrophysics Data System.

REFERENCES

- Belcher, J. W., Davis, L. Jr. & Smith, E. J. 1969, *J. Geophys. Res.*, 74, 2302
 Belcher, J. W. 1987, *Science*, 238, 170
 Blandford, R. D. & Königl, A. 1979, *ApJ*, 232, 34
 Britzen, S. et al 2010a, *A&A*, 515, A105
 Britzen, S. et al 2010b, *A&A*, 511, A57
 Cohen, M. H. et al. 2014, *ApJ*, 787, 151 (Paper I)
 Edberg, N. J. T. et al. 2010, *J. Geophys. Res.*, 115, AO7203
 Fermi, E. 1949, *Physical Review*, 75, 1169
 Gabuzda, D. C. 1999, *New Astronomy Reviews*, 43, 691
 Gabuzda, D. C., Murray, É. & Cronin, P. J. 2004, *MNRAS*, 351, L89
 Gabuzda, D. C. & Pushkarev, A. 2001, in *ASP Conf. Ser. 250, Particles and Fields in Radio Galaxies*, eds R. A. Liang & K. M. Blundell, 180
 Goldreich, P., & Sridhar, S. 1997, *ApJ*, 438, 763
 Gurnett, D. A. & Bhattacharjee, A. 2005, “Introduction to Plasma Physics”, Cambridge, p199
 Gurnett, D. A. & Bhattacharjee, A. 2005, “Introduction to Plasma Physics”, Cambridge, p208
 Hardee, P. E., Walker, R. C. & Gómez, J. L. 2005, *ApJ*, 620, 646
 Hovatta, T., Valtaoja, E., Tornikoski, M. & Lahteenmaki, A. 2009, *A&A*, 494, 527
 Hovatta, T. et al. 2014, *AJ*, 147, 143
 Hughes, P. A. 2005, *ApJ*, 621, 635
 Hughes, P. A., Aller, H. D. & Aller, M. F. 1989, *ApJ*, 341, 54
 Hughes, P. A., Aller, H. D. & Aller, M. F. 1989, *ApJ*, 341, 68
 Hughes, P. A., Aller, H. D. & Aller, M. F. 1991, *ApJ*, 374, 57
 Jorstad, S. G. et al. 2005, *AJ*, 130, 1418
 Kellermann, K. I., Vermeulen, R. C., Zensus, J. A. & Cohen, M. H. 1998, *AJ*, 115, 1295
 Kovalev, Y. Y., Lobanov, A. P., Pushkarev, A. B. & Zensus, J. A. 2008, *A&A*, 483, 759
 Lind, K. R., Payne, D. G., Meier, D. L., & Blandford, R. D. 1989, *ApJ*, 344, 89
 Lister, M. L. & Homan, D. C. 2005, *AJ*, 130, 1389
 Lister, M. L., Cohen, M. H., Homan, D. C., et al. 2009, *AJ*, 138, 1874
 Lister, M. L., Aller, M. F., Aller H. D., et al. 2013, *AJ*, 146, 120
 Lobanov, A. P. & Zensus, J. A. 2001, *Science*, 294, 128
 Lyutikov, M., Pariev, V. I. & Gabuzda, D. C. 2005, *MNRAS*, 360, 869
 Marscher, A. P. & Gear, W. K. 1985, *ApJ*, 298, 114
 Marscher, A. P. 2014, *ApJ*, 780, 87
 McIntosh, S. W., de Pontieu, B., Carlsson, M., Hansteen, V., Boerner, P. & Goossens, M. 2011, *Nature*, 475, 477
 Meier, D. L. “Black Hole Astrophysics: The Engine Paradigm”, Springer, 2012, 717
 Meier, D. L. 2013 in “The Innermost Regions of Relativistic Jets and Their Magnetic Fields”, *EPJ Web of Conferences*, 61, 01001
 Mizuno, Y., Hardee, P. E. & Nishikawa, K.-I. 2014, *ApJ*, 784
 Nakamura, M. & Meier, D. L. 2004, *ApJ*, 617, 123
 Nakamura, M. & Meier, D. L. 2014, *ApJ*, 785, 152
 Murphy, E., Cawthorne, T. V. & Gabuzda, D. C. 2013, *MNRAS*, 430, 1504
 O’Sullivan, S. P. & Gabuzda, D. C. 2009a, *MNRAS*, 393, 429.
 Perucho, M., Lobanov, A. P., Martí, J.-M., & Hardee, P. E. 2006, *A&A*, 456, 493
 Perucho, M., Kovalev, Y. Y., Lobanov, A. P., Hardee, P. E. & Agudo, I. 2012, *ApJ*, 749, 55
 Perucho, M. 2013, *European Physical Journal Web of Conferences*, 61, 2002
 Pushkarev, A. B. et al. 2012, *A&A*, 545, A113
 Raiteri, C. M. et al. 2013, *MNRAS*, 436, 1530

¹⁵ <http://www.bu.edu/blazars/VLBAproject.html>